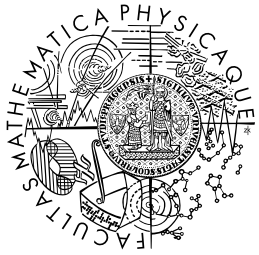

FACULTY
OF MATHEMATICS
AND PHYSICS
Charles University

MASTER THESIS

Mária Zemková

Magnesium alloys designed for medical applications

Department of Physics of Materials

Supervisor of the master thesis: RNDr. Peter Minárik, Ph.D.
Study programme: Physics
Study branch: Physics of Condensed Matter and Materials

Prague 2018

I declare that I carried out this master thesis independently, and only with the cited sources, literature and other professional sources.

I understand that my work relates to the rights and obligations under the Act No. 121/2000 Sb., the Copyright Act, as amended, in particular the fact that the Charles University has the right to conclude a license agreement on the use of this work as a school work pursuant to Section 60 subsection 1 of the Copyright Act.

In ..... date ..... signature of the author

Title: Magnesium alloys designed for medical applications

Author: Mária Zemková

Department: Department of Physics of Materials

Supervisor: RNDr. Peter Minárik, Ph.D., Department of Physics of Materials

Abstract: This Master thesis is focused on the influence of hot extrusion and equal channel angular pressing (ECAP) on the microstructure, mechanical and corrosion properties of magnesium alloys. Investigated materials include three magnesium alloys with the addition of neodymium and/or yttrium elements - N3, W3 and WN43, as a potential material for medical applications. Moreover, the influence of alloying elements in solid solution state was studied. Microstructure development was characterized by scanning electron microscopy together with transmission electron microscopy and X-ray diffraction. Mechanical properties was studied by compression deformation tests in two perpendicular directions and by microhardness tests. The linear polarization method was used to study corrosion resistance.

The processing though ECAP resulted in grain refinement in all three alloys. Ultra-fine grained microstructure was achieved in W3 and WN43 alloy. The high degree of recrystallization during ECAP caused the formation of high-angle grain boundaries in all three alloys. Weak texture evolution was maintained during both processings. A different initial fraction of intermetallic phases before extrusion led to significant changes of microstructure after further processing; nevertheless, the final microstructure after ECAP does not depend on initial microstructure of WN43 alloy. The mechanical properties were substantially affected by the resulting microstructure, mainly grain size and the amount of alloying elements. Thus, the measured yield strength and ultimate strength increased significantly after ECAP processing together with microhardness. The relatively high amount of impurities (iron) in all three alloys probably influenced the corrosion resistance of the solid solution samples of W3 and WN43. The processing through ECAP had almost no or very slightly negative effect on the corrosion resistance of N3 and WN43 alloys; however, the increase of corrosion resistance of W3 alloy after ECAP was measured. We assume that the presence of intermetallic phases in the magnesium matrix in N3 and WN43 had negative effect on initial corrosion attack compared to W3 alloy, where only very small fraction of these phases was observed.

Keywords: magnesium biomedicine ECAP microstructure mechanical properties corrosion

I would like to convey my gratitude to the following people for their aid and support during my work on this thesis. My deepest thanks go to my supervisor Peter Minárik for his guidance and many useful discussions. I appreciate very much his critical reading of the present work, which greatly contributed to its improvement. I would also like to thank doc. Robert Král for preparation of the studied material through ECAP. I also thank Jozef Veselý for the many hours he spent with the TEM observations. And I thank all the other members of the Department of Physics of Materials for the friendly and helpful atmosphere. I would also like to thank Jan Bohlen from Helmholtz-Zentrum Geesthacht in Germany for his X-Ray diffraction measurements. Last but not least my gratitude goes to my very close friend Jan Kotek for his patience and help with grammatical corrections of this manuscript. Finally, I would like to thank the Charles University Grant Agency for financial support under the grant number 250333/2017.

Contents

1. Introduction

1.1 Magnesium and its alloys

Magnesium was first discovered in 1774 and was named after the ancient city of Magnesia [1]. Magnesium ion (Mg^{+2}) is one of the most abundant ions in the oceans. In the Earth's crust magnesium is regarded as the eighth most abundant element. In the nature it is not found in the elemental form, but only in chemical compounds. Silicate olivines, serpentine or talc represent the most commonly occurring natural magnesium compounds. However, more important for industry are the minerals: magnesite ($MgCO_3$), dolomite ($MgCO_3{\cdot}CaCO_3$) and carnellite ($KCl{\cdot}MgCl_2{\cdot}6H_2O$) or minerals from sea water [2]. Pure magnesium metal was first isolated in 1828 by French scientist Antoine-Alexander Bussy [3]. He obtained metallic magnesium by fusion of magnesium chloride with metallic potassium. Currently, magnesium is extracted from molten anhydrous ($MgCl_2$) by electrolysis, from dolomite by thermal reduction or from the aforementioned sea water by extraction of magnesium oxide.

Around 1915 the first commercial production of magnesium started. From this period the research of magnesium for structural applications has continued. New magnesium alloys were introduced; however, the enthusiasm has eroded due to very poor corrosion properties and Mg was replaced by 1.5 times heavier aluminium or steel. Due to the low specific weight, excellent machinability and good recycling potential the interest in magnesium was renewed during the last decades in both aerospace and automotive industries.

Magnesium belongs to the group of alkaline earth metals (second main group in the periodic table of elements). Mg with its atomic number 12 and hexagonal closed-packed (HCP) crystal structure is element of true metallic character but it is non-magnetic. HCP crystal lattice and the major planes of Mg are shown in Figure 1.1. The lattice parameters are $a = 3.18$ Å and $c = 5.19$ Å and the lattice has slightly less c/a ratio than the ideal one of 1.62354 at 25 °C. The density of pure magnesium is 1.738 g/cm^3 at 20 °C and the melting point under atmospheric pressure is 650 ± 0,5 °C.

Magnesium and magnesium alloys exhibit several qualities such as the lowest density of all metallic construction materials, high specific strength or good castability. Many magnesium alloys also offer very good machinability with high cutting speeds and processability; even the most complicated parts can by easily produced. Another interesting aspect is that magnesium alloys have good damping behaviour because of high mobility of dislocations. This is desirable because it results in a reduction of sonic emission and an extension of the life cycle of machines and equipments [6].

Despite their excellent properties, there are some disadvantages that have limited the application of the magnesium alloys. Because HCP structure provides limited number of slip systems, the cold working ability is very poor as well as

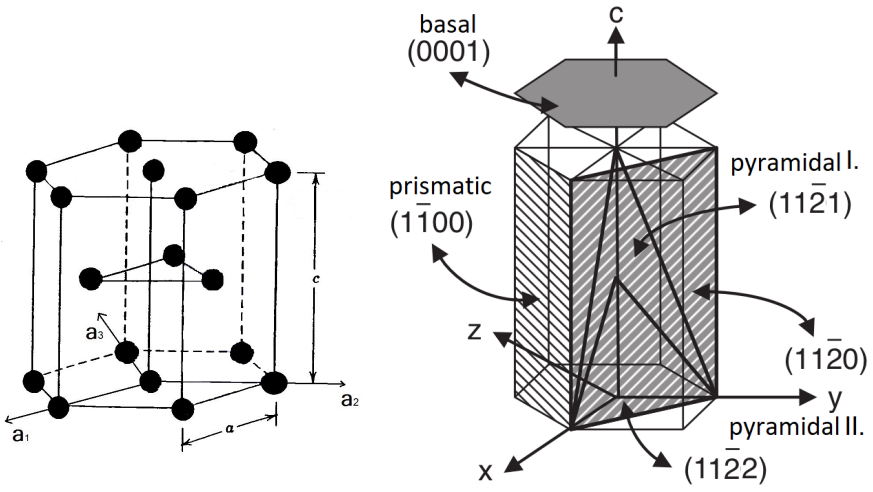

(a) (b)

Figure 1.1: a) The magnesium unite cell [4], b) principal planes of HCP [5].

ductility and toughness at room temperature. Their high-temperature properties such as creep resistance are limited. Besides, magnesium has very high electrochemical reactivity; therefore, corrosion resistance is very low.

Researchers put a lot of effort into the development of magnesium alloys with preferable properties. Furthermore, due to the interest in the use of magnesium alloys in civilian aircrafts, automotive industries or in biomedical applications, there is a need to aquire good mechanical properties and high corrosion resistance of Mg alloys. To achieve this, extensive investigation has been carried out on the composition design and thermomechanical processing of Mg alloys.

1.2 Alloying elements

Pure magnesium is rarely used in structural applications due to its limited properties. It is well known that the physical properties of magnesium can be affected by the amount of alloying elements. This is why there has been a lot of effort to influence the properties of pure magnesium with different alloying elements in order to reduce the negative attributes and enhance the positive ones. Magnesium is chemically active and usually reacts with other metallic alloying elements to form intermetallic compounds. These intermetallic phases influence the microstructure and thus widen the range of material properties.

First, it is necessary to note that the identification of magnesium alloys is standardized. Each alloy is marked with letters that indicate the main alloying elements. The letters are followed by numbers representing the percentage of the given element the alloy contains.

Among the magnesium alloys, AZ and AM series with aluminium (A) and zinc (Z) or manganese as the principal alloying elements have been commonly used for many decades. These alloys attained good strength and corrosion resistance [7],

[8]. Currently, the progress of Mg alloy development has been connected with the use of rare earth metals as alloying components. The rare earth elements (RE, for identification in Mg alloys is used mark E), including yttrium (Y, in alloy series marked as W), have become more and more popular since they could significantly increase strength. Due to the high cost, these elements are mainly used as rare-earth mischmetal (Mischmetal is a natural mixture of rare earth elements).

All rare earth elements form eutectic systems thus, precipitation strengthening is possible. Precipitations are very stable at elevated temperature [9] and increase the creep resistance and high-temperature strength [10]. Some papers [11, 12] reported promising results in terms of weakening the texture and improving the deformability of Mg. Moreover, RE elements also have a positive influence on the corrosion resistance [13, 14]. Further development of these alloys led to the introduction of the commercially very successful Mg based series WE. Such alloys contain Y, RE and a small amount of zirconium is added for a better grain refinement. The WE series represents alloys with good castability, which are heat resistant (up to 300°C), highly creep resistant and corrosion resistant. At the present time, the WE alloys have characteristic profile comparable to aluminium alloys. One of the representative alloys of WE series is commertially very succesful Magnezix. This alloy has recently been proposed for the manufacture of the first class of functional biodegradable magnesium implants [15].

The RE metals form a group of elements with similar chemical properties. Nevertheless, the investigations [14, 16] show different effects of each RE elements on the properties of Mg. Different results confirmed that two common RE elements, neodymium and yttrium, if used at low concentrations, are suitable alloying elements for magnesium alloys causing no negative effects on cell viability *in vitro* test systems [17], [18], [4]. Thus, such alloys are considered a promising biological material.

As discussed above, one of the promising alloying components in commercial Mg alloys is Neodymium (Nd). Neodymium has the highest solid solubility among the rare-earth elements [19] and because of its low eutectic temperature ($\sim$ 550°C) it has a very good response to age hardening. Moreover, increasing the content of Nd causes a grain refinement of Mg alloys [20]. It was also found that the creep resistance increases with the increasing amount of neodymium [21]. The investigation about corrosion properties of magnesium alloys containig Nd indicated that the corrosion resistance of these alloys can be enhanced by optimal concentration of Nd [22].

Yttrium has been tested by many researchers because of the large difference in the atomic radii of Mg (145 pm) and Y (212 pm), due to which strengthening of Mg by solid solution strengthening and precipitation strengthening is possible. The improvement of the strength by solution strengthening effect of Y has been demonstrated, however, at the expense of ductility [23]. Yttrium also acts as a great grain refiner [24], which positively influences the mechanical properties. Some reports indicate that corrosion resistance of Mg alloys could be increased by Y, but it strongly depends on the composition ofthe Mg alloy and the percentage

of content of Y [4].

The investigation of binary systems is crucial for understanding of the role of individual alloying elements on the pure magnesium materials. Still, only one doping element is often insufficient and more than two elements are added to achieve required properties. An existing investigation [25] of the constitution of RE elements reported that when two or more kinds of RE elements are added, the interaction between them can reduce their solubilities in the Mg matrix. By addition of the proper amount of the alloying elements one can influence the wide spectrum of material properties.

1.3 Mechanical properties

The mechanical properties such as compression or tensile stress of the magnesium materials depends on the chemical composition, conditions of thermomechanical processes, heat treatment and other factors. As has already been mentioned, alloying with different elements is very common. Furthermore, within the same composition, the mechanical properties can vary considerably with the subsequent type of thermomechanical processing.

Generally, the main mechanism for improving the mechanical properties of alloys is grain refinement (1), precipitation hardening (2), solid-solution hardening (3) and work hardening (4).

1. The average the grain size of a material generally plays a very important role, often the dominant. Thus, the strength of all polycrystalline materials is related to the grain size, d. According to the Hall-Petch Equation (1.1)

$$\sigma = \sigma_0 + \frac{k}{\sqrt{d}}, \tag{1.1}$$

   the strength of material increases with grain size reduction. σ represents the deformation stress (yield stress), σ_0 is the friction stress necessary for the dislocation motion in the lattice and k is the Hall-Petch constant specific to the material.

2. The precipitation reaction is a diffusive transformation process involving the formation of second phase particles from the supersaturated solid solution. The effectiveness of precipitation strengthening depends on the reduced solubility of the alloying elements at low temperature as well as on the amount of the precipitated phases and their stability at elevated temperature. Precipitates are a significant barrier for the dislocation motion. A higher degree of precipitation hardening is obtained with finer particles and larger number density together with a homogeneous distribution.

3. Solid-solution strengthening is characterized by the complete dissolution of the alloying elements in the magnesium lattice. The solute atoms in magnesium prefer substitute position at the base lattice. These atoms provide

strengthening by atomic misfit introducing local lattice strain which forms a barrier for the dislocation motion.

4. Work hardening is a strengthening method of the material during plastic deformation at low temperature. When the material is deformed the strengthening occurs because of the dislocation motion and dislocation generation within the crystal structure of the material. This way a further dislocation motion is suppressed and higher flow stress is needed for further deformation.

1.3.1 Precipitation strengthening phases

Many magnesium casted or wrought alloys achieved their useful mechanical properties via precipitation strengthening. This involves controlled decomposition of supersaturated solid solution into a fine distribution of precipitates in the magnesium matrix [26]. This process often involves the formation of a series of metastable or equilibrium precipitates phases. Therefore, it is important to control the precipitation when the maximum precipitation effect should be achieved [26].

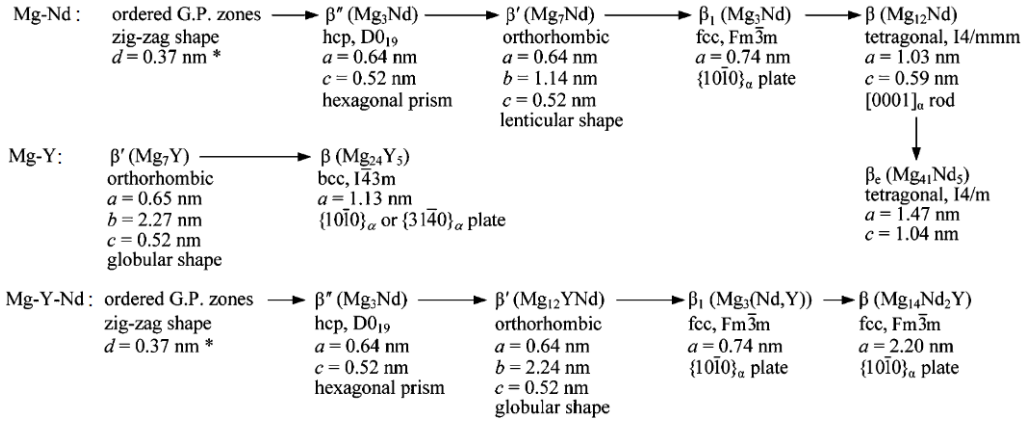

Figure 1.2: The precipitation sequence of three magnesium alloy systems [26].

Because magnesium alloys can form secondary phase particles during thermomechanical processing it is important to introduce the precipitation sequences of some of them. As has already been noted, alloys with neodymium and yttrium are promising structural materials, thus their precipitation sequences will be described. The series are provided in Figure 1.2. It is known that the age hardening response of Mg-Y-Nd alloys is much higher compared to other binary alloys. This sequence starts with the $\beta^{\text{“}}$ phase, which is metastable and fully coherent with Mg matrix. During aging temperature from 200 to 250° $\beta^{\text{‘}}$ phase is formed, which is also metastable phase. It also seems that $\beta^{\text{‘}}$ phase formed in Mg-Y alloy is similar to $\beta^{\text{‘}}$ in Mg-Y-Nd [27]. The precipitation sequence ends with β equilibrium phase, which develops in a FCC (face center cubic) structure [28]. The next sequence of Mg-Y ends with an equilibrium β phase, which has the composition of $Mg_{24}Y_5$. An almost identical precipitation sequence has been reported for Mg-Nd binary alloy and for Mg-Y-Nd. But β phase with a composition

of $Mg_{12}Nd$ has a body-centered tetragonal structure and it is a metastable phase [26]. The final precipitation phase of Mg-Nd alloy is β_e phase. This equilibrium precipitate phase was identified as $Mg_{41}Nd_5$.

1.4 Plastic deformation of magnesium

Magnesium, due to the HCP structure which involves a limited number of slip systems, exhibits a different deformation behaviour in comparison to materials with a cubic lattice. Generally, a slip deformation mechanism is predominant during plastic deformation and it is realized by motion of the dislocations. The slip most likely occurs in the densest crystalline planes and in the directions with the largest density of atoms. The slip planes and slip directions form so-called slip systems. During the plastic deformation a large amount of dislocations move in different slip systems and cause permanent shape changes of the crystal lattice. Which slip system will be activated depend on their specific critical resolved shear stress (CRSS). Thus, the slip occurs when the stress acting on the slip plane in the slip direction reaches a certain critical value of CRSS. The relationship between the shear stress resolved on the slip plane, the applied stress σ and the orientation of the slip system upon uniaxial loading is defined by Schmid's law (1.2):

$$\sigma_{CRSS} = \sigma m = \cos\phi \cos\lambda, \tag{1.2}$$

where m is a geometrical factor (Schmid factor), ϕ is the angle between the normal of the slip plane and the direction of the applied force and λ is the angle between the slip direction and the direction of the applied force.

According to Schmid's law the orientation of the crystalline lattice plays an important role in the deformation behaviour. Thus, the development of the texture in polycrystalline material can change the deformation behaviour of the material. But also vice-versa, the deformation of the material can change the orientation of the grain lattice and form a new, random texture.

According to the Von Mises criterion, at least five independent slip systems are necessary for a homogeneous plastic deformation in a polycrystalline material. It is well known that during plastic deformation of Mg only four slip systems are activated: basal (0001), prismatic $(10\bar{1}0)$, pyramidal of first class $(10\bar{1}1)$ and pyramidal of the second class $(11\bar{2}2)$ [29]. Therefore, an additional mechanism is supposed to play an important role. This mechanism is mechanical twinning. Twinning modify the original lattice by gliding or sliding along the planes between rows of atoms.

Accordingly, mechanisms of the plastic deformation commonly encountered in Mg based alloys include dislocation glide, deformation by twinning plus grain boundary sliding. Moreover, dynamic recrystallization also occurs in the material. The determination of which deformation mode is activated depends on the volume of each mode that is stressed and on the magnitude of the critical stresses, that is necessary for the activation to occur.

1.5 Material processing

Mechanical and physical properties of all crystalline materials can be altered and improved via adjustment of several factors: grain size, precipitation, texture, dislocation density. These factors are generally modified by specifics applications of pre-determined thermomechanical treatments in which the material is subjected to specific temperature regimes and mechanical strain. At past a lot of attention has been directed towards the development of new technique that may be used to achieve material with advanced and unique properties.

In practice, one of the most extensively used metal working procedures is extrusion. However, the extrusion proces has a limited ability to produce material with required qualities. This is why severe plastic deformations (SPD) are additionally used. These techniques include equal-channel angular pressing (ECAP), high-pressure torsion (HPT), twist extrusion [30] and many more. Formally, the SPD metal working imposes a very high strain in the bulk material without the significant change in a dimension of the working piece.

1.5.1 Extrusion

Extrusion is the metal forming process in which a rod-like piece of material with a certain cross section is pushed through a die of a smaller cross section. The basic principle of extrusion is illustrated in Figure 1.3. The important parameters of the extrusion are a working temperature, a speed of extrusion ram and an extrusion ratio (ER), defined in Equation (1.3):

$$\mathrm{ER} = \frac{\mathrm{S_0}}{\mathrm{S_1}}, \tag{1.3}$$

where S_0 is the initial cross section and S_1 is the final cross section. This parameter is highly dependent on the working temperature; higher temperature allows higher extrusion ratio.

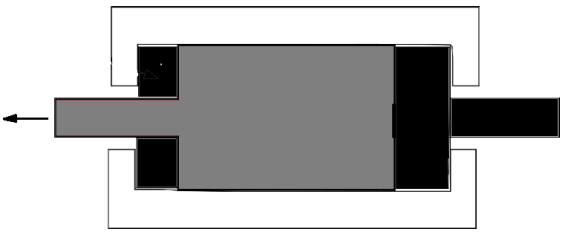

Figure 1.3: The configuration for the direct extrusion processing.

Like any metal forming processes, it can be performed either cold or hot. Hot forming is performed above a recrystallization temperature of processed material which has many advantages. As-cast materials usually contain pores and vacancies, these can be closed up by pushing and redistributing the material during extrusion. High temperature causes break up of irregular structures or impurities. However, sometimes too high temperature with improper choice of other extrusion parameters can create elongated grains along the extrusion direction,

considered negatively.

The deformation during extrusion process usually leads to the recrystallization of the mass of material into a finer grain structure and to formation of special texture development. For magnesium alloys is typical when c-axis is aligned perpendicular to the extrusion direction.

1.5.2 Equal-channel angular pressing (ECAP)

From the various types of the SPD, the ECAP is the most extensively used processing technique to fabricate bulk of an ultrafine grain (UFG) microstructure. The ECAP is relatively new metalworking process, compared to rolling, firstly introduced by Segal and his co-workers. The principle of conventional ECAP process is schematically illustrated in Figure 1.4*a*. A material in a shape of bar or rod is pressed through a bent channel. The channel is characterized by two angles: Φ which represents the angle between channels and Ψ which represent a deviation from the sharp edge of the outer corner. Because the cross section of samples do not change, the same sample may be pressed repetitively. For the samples with square or circular cross-section it is convenient to rotated the billets about 90° between each pass.

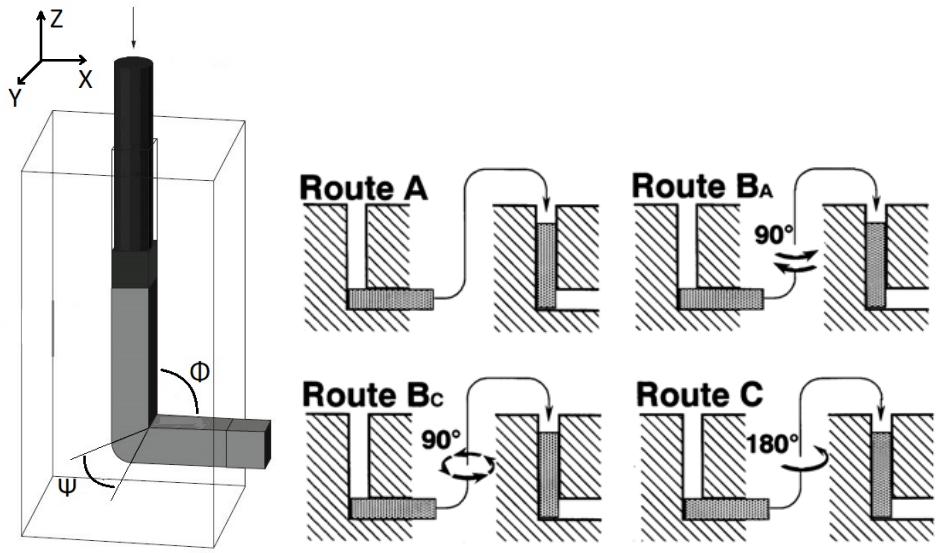

(a) (b)

Figure 1.4: a) The configuration for the ECAP processing, b) the four fundamental processing routes in the ECAP [31].

Generally, we recognise four fundamental processing routes in the ECAP, summarized schematically in Figure 1.4*b*. Thus, in route A the sample is pressed repetitively without any rotation, in route B_a the sample is rotated by 90° alternatively between consecutive passes, in route B_c the samples is rotated by 90° in the same direction between each pass. At last, in route C the sample is rotated

by 180° between each pass [31]. But, various combinations of these routes are also possible.

The nature of the impressed deformation during one pass is a simple shear. It is evident that the deformation occurring in subsequent pressing will depend upon the character of any rotation of the sample. Hence, with the different processing routes different slip planes are activated and different character of microstructure can be achieved. For routes mentioned before these slip planes are illustrated in Figure 1.5. The planes are labelled from 1 to 4, which corresponds to the first four passes of the ECAP. It is necessary to mention that the B_c route was found to be the most effective route to achieve the uniform ultrafine grain microstructure with a rapid evolution of a high-angle grain boundaries in each of the three orthogonal planes [32].

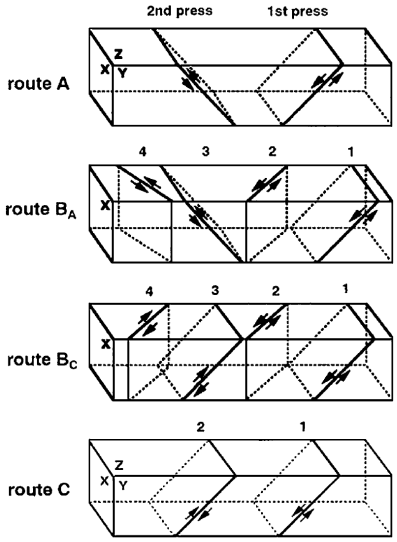

Figure 1.5: The active slip systems for consecutive passes [31].

During the ECAP process, several different factors influence the workability and the characteristics of the final microstructure. Firstly, there are factors associated with geometry of the die, such as the values of angles Φ and Ψ. It was reported [33] that the ultrafine equiaxed grains were easily achieved when the die had angle Φ of 90° because very intensive plastic strain was imposed compared to higher Ψ. This strain can by generally expressed in the form (1.4):

$$\epsilon_N = \frac{N}{\sqrt{3}}\Big[2\cot\Big(\frac{\Phi}{2}+\frac{\Psi}{2}\Big)+\Psi\csc\Big(\frac{\Phi}{2}+\frac{\Psi}{2}\Big)\Big], \tag{1.4}$$

where N is number of the ECAP passes.

Secondly, there are factors associated with processing regime, which includes the operation temperature, the speed of pressing or the presence or absence of back pressure. However, due to the low ductility of magnesium alloys, the processed temperature is usually higher. Accordingly, the tendency to recrystallization and to grain growing during higher pressing temperature can be observed.

Thus, the operation temperature is a key factor for stabilize the grain size.

It is also important to recognize that the microstructure may be also significantly influenced by the ECAP parameters in another way. The high pressure involved during pass may lead to a breaking and fragmentation of secondary phase particles. Moreover, these small broken phases can be redistributed in the matrix as was reported in paper [34], where ECAP effectively disrupted the secondary phases aligned in a stripes after the extrusion. Another dominant attribute of the ECAP is a potential to induce unique predominate crystallographic orientation and thus impact the structural properties of processed material.

1.6 Corrosion properties

In the last few years alloy development was focused not only on the improvement of the mechanical properties, for instance ductility or strength but also on corrosion properties. In many aspects, a corrosion resistance plays very important role in the current research of the magnesium alloys. From the technical point of view, the corrosion protection must be ensured especially for the magnesium alloys twice more.

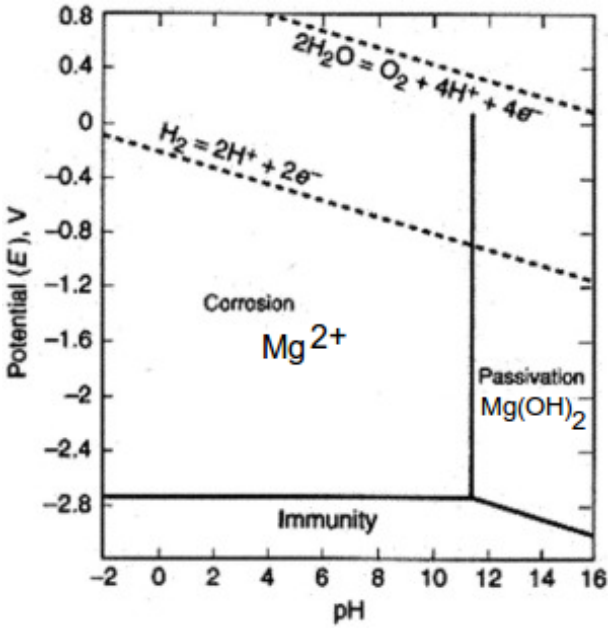

Figure 1.6: Potential-pH (Pourbaix) diagram for the system Mg-water at 25 °C [35].

When a freshly prepared surface of the pure magnesium is exposed to the air or water at room temperature, the material has a tendency to corrode due to a reaction with surrounding media. The corrosion process occurs because the material strives to return to the oxidized natural state. However, the metal can or can not corrode under the certain circumstances as illustrates potential-pH diagram for Mg in the moist environment, also called Pourbaix digram (Figure 1.6). The Pourbaix diagram of pure Mg shows theoretical domains of the corrosion, immunity and passivity. As can be seen from the diagram Mg corrode in relative wide range of the potential and pH. In this region, magnesium dissolves as Mg^{+}

and Mg^{+2} with accompanying hydrogen evolution due to the dissociating water.

The following reactions (1.5) - (1.7) take place:

$$Mg \rightarrow Mg^{2+} + 2e^{-}, \tag{1.5}$$

$$2H_2O + 2e^{-} \rightarrow H_2(g) + 2OH^{-}. \tag{1.6}$$

$$Mg^{2+} + 2OH^{-} \rightarrow Mg(OH)_2. \tag{1.7}$$

The corrosion product of magnesium hydroxide $Mg(OH)_2$ can be readily develop on metallic surface even at acid pH values (region of corrosion), but is thermodynamically unstable and porous. The Mg is exposed and the hydrogen evolution present during the corrosion causes further corrosion and the separation of the hydroxide layer. According to the Pourbaix diagram, the protective layer of $Mg(OH)_2$ is stable only in the alkaline conditions, with pH above 10.5. Because in practice there are no options to alter the environment, the main way how to control the corrosion properties is manipulation with the chemical composition and the microstructure. However, in the magnesium alloy development, a microgalvanic corrosion often becomes very excessive due to impurities (Fe, Cu, Ni), crystallographic defects or the alloying elements. The difference of the electronegative potentials between the Mg matrix and the impurities accelerates the galvanic corrosion and significantly decrease the corrosion resistance.

The addition of the certain elements into the Mg matrix is supposed to prevent the microgalvanic processes and to allow the formation of the stable cover layer. The specific elements are also rare earth elements. The Nd or Y exhibit close electrochemical standard potential to Mg, thus the extent of galvanic corrosion is lower.

Generaly, there are many external or internal factors that influence the rate and distribution of the corrosion. One of the most important external factors are: composition of the solution (inhibitors or stimulants), temperature of solution and rate of the solution movement. These factor are more or less well controlled during the experimental tests. Internal factors include the chemical compositions of the corroding material, internal stresses, surface conditions and microstructural characteristics such as homogeneity and distribution of the intermetallic phases, grain size and character of the grain boundaries. However, these internal factors are often difficult to control.

The influence of different thermomechanical processing such as extrusion, ECAP or post-annealing treatment has a potential to greatly influence the factors connected with the microstructural properties e.g. grain size, precipitation character, dislocation density, texture and to affects corrosion resistance of the Mg alloys. Many researchers demonstrated that the grain refinement affects the corrosion resistance. However, their studies are often contradictory. Another very crucial factor concerns the intermetallic phases. Distribution and character

of these precipitates are strongly influenced by solid solubility of alloying elements and by thermo-mechanical treatment. The SPD process such as ECAP inserts into the material severe strain which leads in many cases in the fragmentation and homogeneous redistribution of intermetallic phases. Homogeneously distributed phases often result in the improvement of the corrosion resistance due to the formation of more stable protected layer. Moreover, some report [36] demonstrated the influence of the grain orientation on the corrosion properties. Thus, the texture evolution during different thermomechanical treatments could also play a role.

1.7 Magnesium in medicine

Magnesium is presented naturaly in the human body in the form of ions. More than a half of the total amount is present in a bone tissue [37]. It also takes part in many human metabolic reactions and is essential for healthy function of the human body and living organisms. Because Mg is not toxic, Mg and its alloys posse's great potential for the application of biodegradable medical implants.

Surprisingly, the concept of using magnesium as an implantable material is not so young. In the first decades of the 20th century, magnesium was studied for several medical applications. But the more rapid progress of a stainless steel as the metallic implants displaced magnesium from this field. At the last three decades the studies of Mg and its alloys as the bioimplants have become a booming research area.

Because Mg has similar mechanical properties compared to the natural bones and lower densities compared to other metallic biomaterials, such as titanium alloys or stainless steels, Mg alloy are becoming very attractive. Mg alloys exhibit an elastic modulus similar to that of the human bone, which prevents the human bone against the stress shielding. As degradable materials, Mg alloys serve as material for the temporary implants which degrade *in vivo* and they are replaced by new bone tissue. This fact eliminates the need for a second surgery for removing the implant from human body and significantly decreases the medical costs and further torment of the patient. Moreover, an illimitable property of magnesium is its excellent biocompatibility.

In many ways rapid corrosion rate of magnesium in the aqueous environment complicates the potential applications of Mg based alloys. Rapid degradation of Mg alloys results in a quick decrease of the mechanical properties that can lead to a collapse of the implant before the recovery. Furthermore, the hydrogen gas that is formed during the corrosion process can lead to negative tissue reactions followed by a pain. Last but not least, carefully chosen alloying elements is necessary. In many cases, metallic ions are not perfectly biocompatible and can affect a tissue healing. In order to overcome these deficiencies thorough research has to be done.

Despite all this, the world's first bioabsorbable metallic material for implants was introduced. MAGNEZIX® is an aluminium-free magnesium alloy that is

classified as an Mg-Y-RE-Zr alloy. This alloy contains rare earth elements and more than 90 wt.% of the magnesium and it is compositionally similar to WE43 magnesium alloy. It has already demonstrated good biocompatibility and osteoconductive quality *in vivo* [38].

2. Motivation and objectives

Development of magnesium alloys has traditionally been driven by automotive and aerospace industry, which require lightweight materials. Magnesium alloys have been attractive due to their low density, superior mechanical strength to weight ratio and environmental friendliness. However, another interesting quality of magnesium has been intensively studied during last three decades. Biocompatibility and biodegradability of magnesium increased interest of its alloys in a field of medical applications. Meanwhile, small volume implants and degradable coronary stents have already been clinically tested. However, the use of larger implants is still limited due to the rapid corrosion leading to the hydrogen accumulation in the surrounding area and too rapid deterioration of mechanical properties.

The classical approach to alter the material properties is based on an optimization of chemical composition of the alloys. From the wide spectrum of the magnesium based alloys, very promising seem to be alloys contain the rare earth elements. Different alloying components with a combination of two termomechanical processes bring us opportunity to prepare the material with unique microstructure which hopefully, positively influence properties of the studied alloys.

The objective of the present work is to study an influence of two thermomechanical processes on the magnesium alloys with different content of neodymium and/or yttrium, as a potential materials for the biodegradable applications. The investigation can be divided into following sections:

- The microstructural observations of alloys prepared by hot extrusion and different number of ECAP passes, with attention onthe grain size distribution, character and distribution of the secondary phase particles, character of the grain boundaries.
- The observation of evolution of the mechanical and corrosion properties after the extrusion and the ECAP process.
- The discussion of relations between the microstructure development after the extrusion and the ECAP with evolution of the mechanical and corrosion properties.

3. Experimental methods

3.1 SEM

Scanning electron microscope is a type of microscope that uses a focused beam of accelerated electrons for an imaging and analysis a sample surface. The SEM detects primarily two types of signal, backscattered electrons (BSE) and secondary electrons (SE). The BSE signal occurs due to an elastic interaction of the electrons with atoms of sample, which cause only a change of electron trajectory. The intensity of BSE is proportional to Z number of these atoms. Thus, this signal helps to distinguish between different phases. The BSE signal can be also used to determine a crystallographic orientation of individual grains. This technique is called electron backscatter diffraction (EBSD). The EBSD data provides many microstructural features such as texture, grain size and its distribution, misorientation of grain boundaries. In contrast, the SE signal occurs due to an inelastic interaction between the primary electron beam and the sample. This signal gives us an information about a topography of sample's surface. The variations in electron signal intensity collected at each point (pixel) result in the formation of an image. Another useful signal which can be a product of the electron-matter interaction is X-ray. The characteristic x-ray depends on the atomic number which is unique for every element. Thus, energy disperse x-ray spectroscopy (EDX) can be used to identify the elements that are present in the sample.

Zeiss Auriga Compact scanning electron microscope equipped with the EBSD camera was used for the microstructural observations. The EBSD images were obtained with dimensions of 100x100 µm and with the step size of 0.1 µm for samples processed through ECAP and 1x1 mm with the steps of 0.5 µm for extruded samples. The results were analysed using an OIM analysis software. Each EBSD dataset was cleaned using one step of confidence index standardization and few steps of grain dilatation. These cleaning steps are explained well in report [39].

A very important factor influencing quality of the resultant image obtained by the SEM is quality of the scanning surface. Thus, the samples were cut and firstly mechanically grinded on abrasive papers of grade 1200, 2400 and 4000, individually. Then the samples were mechanically polished with diamond suspensions of grade 1 and 1/4 µm, individually. For the final preparation were used either ion-polisher Leica EM RES102, or electrochemical polisher Struers Electropol with AC2 electrolyte.

3.2 TEM

Transmission electron microscope is a type of microscope where the electron beam of high energy is transmitted through a very thin sample. An image is formed by the interaction of the electron beam with the sample. The beam is then focused onto a fluorescent screen or a charge-coupled device (CCD) camera. TEM has an ability to provide almost all of the structural, phase and crystallographic data of material. The TEM has two modes of operation. In the image observation mode

areas of an different contrast are generated due to the different absorption of electrons in the sample, the absorption depends on a thickness and composition of the material. Chemical mapping can also be performed on this instrument. In the second diffraction mode a diffraction pattern is projected because of the interaction of the electrons with crystal potential of material and an information about a space symmetry or crystal orientation can be obtained.

Many conventional transmission electron microscopes are equipped with additional scanning coil and detector which allows it to switch in the operation mode called scanning transmission electron microscope (STEM). Images are formed similarly like in the TEM by electrons passing through a thin specimen, but in STEM the electron beam is focused to a small spot (0.05 - 0.2 nm) which scanned the sample in a rasters. This mode allows to make a high resolution images with identification of individual atoms columns.

Jeol 2200FS TEM was used with applied accelerating voltage 200 kV. For observation we prepared small and approximately 1mm thin samples that were cut from billets perpendicularly to the extrusion direction. The slices were mechanically grinded from both sides to the thickness of 100-150 µm. 3 mm disks were then cut out of the thin slices. Finally, electrochemical polishing was used on Struers Tenupol 5 in a solution of a perchlorate acid with methanol to obtain the thickness of ∼100 nm, which is transparent for the electrons.

3.3 Texture measurements

An evolution of a texture was measured by the X-ray diffraction. The texture was analised from pole density distribution (pole figures). These pole figures are measured by recording the intensity distribution of a single (hkl) reflection by tilting and rotating the sample over orientation sphere [40].

The X-ray Panalytical^{TM} diffractometer using CuKα radiation was used to measure pole figures on polished cross section of the extruded and ECAPed samples. The measured pole figures were (0002) and $(10\bar{1}0)$, $(10\bar{1}1)$. Samples were cut from the billets into 5 mm slices and polished gradually till 1/4 µm.

3.4 Compression deformation tests

Evolution of the mechanical properties was investigated by compression deformation tests. The deformation tests were performed by INSTRON 5882 deformation device. The tests were carried out in two directions – along processing direction (X) and transverse direction (Y). Tests were performed at room temperature using a constant deformation rate of 10^{-3} s^{-1}. For the tests, bars of 4x4x5 mm^3 were cut from the billets. Investigated parameters were yield strength (yield point) and ultimate strength. At least four measurements were performed for each studied state.

The compressive deformation tests provided characteristics of applied force vs. displacement for each measurement. These characteristics were recalculated to obtain the true stress-true strain curve according to Equations (3.1) and (3.2). The true stress of the sample was determined as:

$$\epsilon = \ln \left| 1 - \frac{\delta l}{l_0} \right|, \tag{3.1}$$

and the true stress of the material as:

$$\sigma = \frac{F}{S_0} \ln \left(1 - \frac{\delta l}{l_0}\right), \tag{3.2}$$

F represents an applied force, S_0 is an initial cross section of the sample, l_0 is an initial length of the sample.

3.5 Microhardness

Microhardness test is useful method to investigate potential hardness gradient of the sample along cross section after different stage of the thermomechanical processing. Moreover, it is a complementary method to examine an evolution of the microstructure homogeneity and its dependence on increasing number of the ECAP passes.

The microhardness tests were performed by fully automatic testing device QNESS Q10a. Vickers indenter applied load of 0.1 kg for 10 s for all measured circles. At least 200 indents were measured for each investigated state. The samples were cut from billets and embedded in the epoxy resin for better manipulation. The samples were polished gradually till 1/4 µm.

3.6 Linear polarization tests

Evolution of corrosion properties of the the investigated alloys were measured by a linear polarization method. The measurements were controlled by a potentiostat Autolab PGSTAT128N^{TM}. All tests were performed in a 0.1 M NaCl solution and an additional rotation of 300 rpm of the sample was introduced to obtain better homogeneity of the measurement.

The linear polarization tests were carried out by a three electrode cell with a power supplied from the potentiostat. The experimental arrangement is schematically illustrated in Figure 3.1. The potentiostat accurately control the potential of the counter electrode (CE) against the working electrode (wE) in the way that the potential difference between the wE and the reference electrode (RE) is well defined. This way we are capable to control cathodic/anodic reaction on the sample surface. At the beginning, as soon as the sample is immersed, the potential between the wE and the reference electrode (also marked as saturated calomel electrode - SCE) is monitored. Open circuit potential (OCP) is estimated after 10 minutes. Subsequently, the wE is polarized in both anodic and cathodic direction with potential range -150 mV - 200 mV with respect to the value of OCP

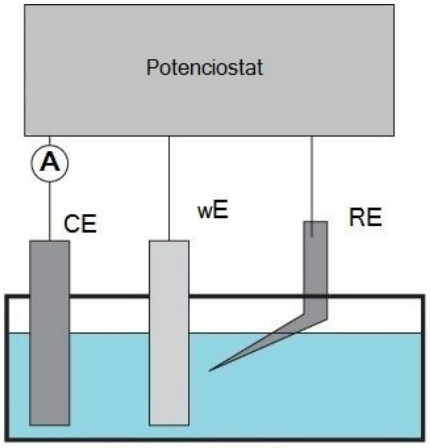

Figure 3.1: The three electrodes setup.

with the constant scan rate of 1 mVs^{-1}. Thus, the degree of the polarization is defined as the overpotential (η) and is given by equation (3.3):

$$\eta = E - E_{corr}, \tag{3.3}$$

where E is a potential of wE for some current flow and E_{corr} is OCP. During the test electric current density i needed for polarization and potential E, are recorded. The typical plot (Evans diagram) illustrates Figure 3.2*a*. In practice, the value of polarization resistance R_p can be directly evaluated from the plot of i and E as an inverse slope of tangent, illustrated in Figure 3.2*b*.

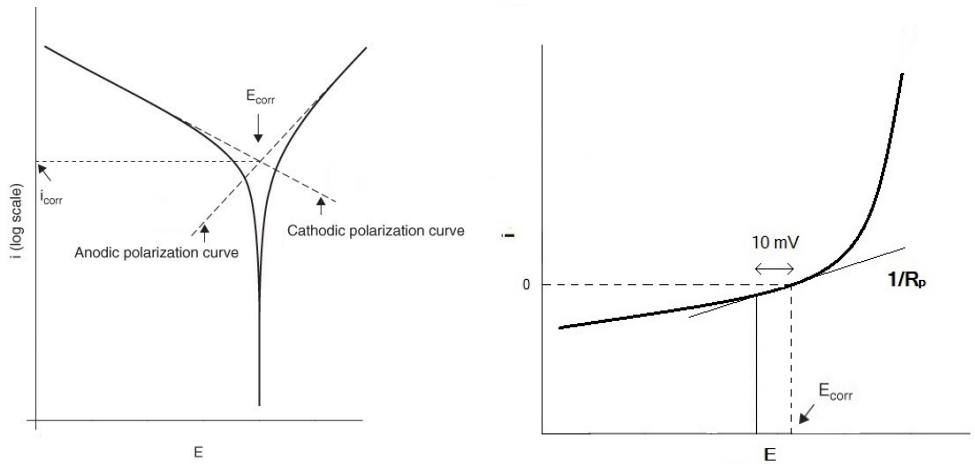

(a) (b)

Figure 3.2: a) The Evans diagram, b) polarization resistance evaluation.

The linear polarization method is a fast technique to evaluate the corrosion properties and is designed for measurement of the polarization resistance. This physical parameter is able to give a available information about corrosion resistance of the material. Therefore, high R_p of the metal implies high corrosion

resistance and low R_p implies low corrosion resistance [41].

No special preparation of the samples is needed. The samples for the corrosion testing were cut from the billets. An upper layer of lubricant contamination and microcracks were removed. consequently the sample were embedded in the nonconductive epoxy resin. In the center of resin was bored a hole for connection with the electrode device of potenciostat. Before each measurement the corroded layer was abraded with the 1200 grid emery paper.

4. Material characteristics

Three magnesium alloys N3, W3 and WN43, that contained neodymium (N) and/or Yttrium (W) were studied in this investigation. The composition of each alloy was acquired by a spark emission spectroscopy and it is shown in Table 4.1. All three alloys were conventionally as-cast and afterwards processed by a hot extrusion. The extrusion process was conducted at 350 °C and was performed with a constant ram speed of 1 mms^{-1}. A diameter of the extruded die was 15 mm and ER = 30. Prior to the extrusion an homogenization annealing was applied for 16 hours at 400 °C for W3, WN43 and 550 °C for N3 alloy, respectively.

	Y	Nd	Fe	Cu	Ni	Mg
N3	-	2,43	0,030	0,0016	0,0014	balance
W3	3,33	-	0,031	0,0037	0,0002	balance
WN43	3,46	3,53	0,0344	0,0039	0,0011	balance

Table 4.1: Composition of the investigated alloys (wt.%).

Rectangular billets were machined from the rod like extruded bars and processed by ECAP. The processing was performed at the temperature range 290-330°C and at the ram speed of a range 5-10 mms^{-1}. The angle Φ between two intersecting channels and the corner angle Ψ were 90° and 0°, respectively. Both channels had a square cross section of 10x10 mm^2. Molybdenum disulphide grease was used as a lubricant. Samples after one pass (1P), two passes (2P), four passes (4P) and eight passes (8P) were prepared following a route Bc.

Although both binary alloys have similar weight percent of the alloying element, there is twice as much atoms of yttrium than neodymium. The marking WN43 of ternary alloy was chosen due to very similar composition of well-known WE43 alloy.

4.1 Annealing treatment

In order to examine an influence of the alloying elements on corrosion properties an annealing treatments were carried out. The annealing treatment was applied on all investigated extruded alloys for 16 h at 525 °C (T4) in an argon atmosphere and quenched in a water. This temperature is standard homogenisation temperature used for WE43 alloy. The samples treated by this temperature were marked as Ex-T4. Additionally, one extruded WN43 sample was annealed with the same conditions and afterwards processed by the ECAP (marked as T4-8P), to examine the influence of solid solution treatment on precipitation processes during the ECAP.

5. Experimental results

5.1 The microstructure after extrusion

Microstructure of all three alloys was studied by EBSD. Representative micrographs of the as-extruded materials in the plane parallel to the extrusion direction are presented in Figure 5.1. In N3 and WN43 alloys we observed fully recrystallized microstructure with high angle grain boundaries (HAGB). Both alloys represent uniform distribution of grains. In the case of W3 the microstructure was partially recrystallized but only small fraction of prolonged grains was presented.

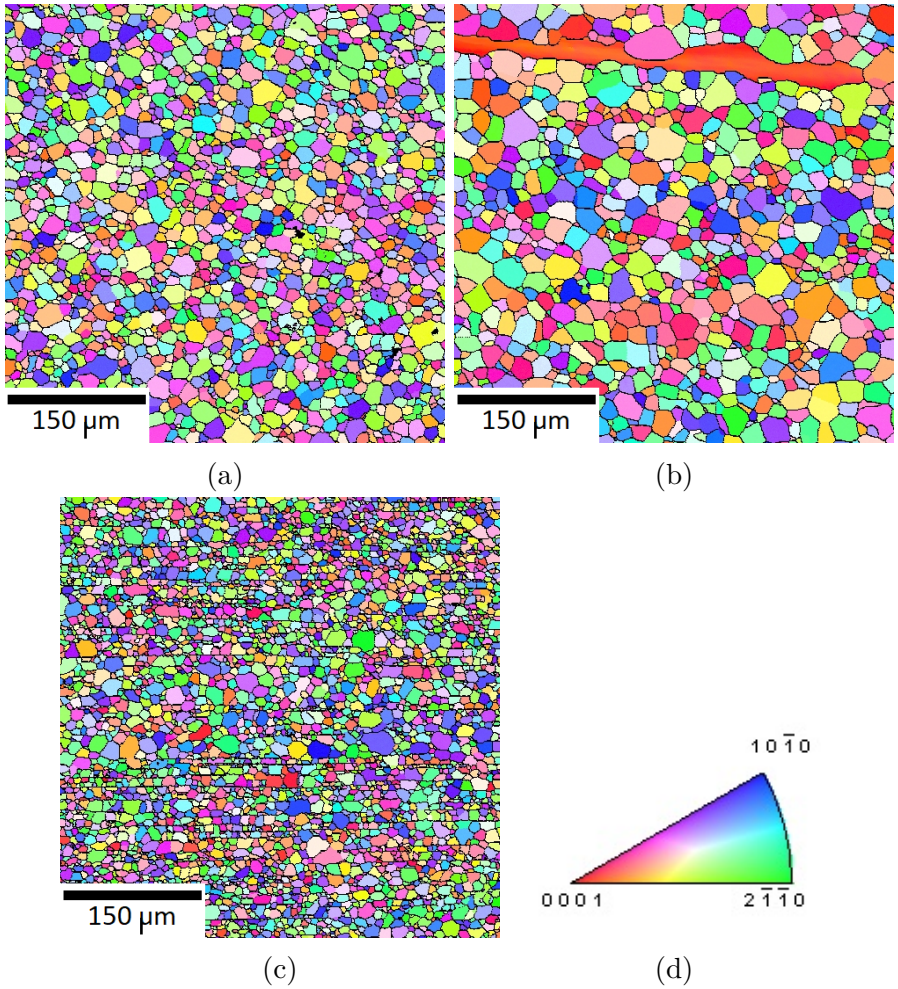

Figure 5.1: The EBSD micrographs of the extruded samples a) N3, b) W3, c) WN43 and d) orientation triangle.

The extrusion led to the highest grain refinement in case of the WN43, where average grain size was about 10 µm and the lowest in case of the W3, where average grain size was about 20 µm. The average grain size of the N3 was around 15 µm.

Figure 5.2 represents (0001) pole figures measured by X-Ray diffraction for all extruded alloys. It can be seen that the typical "rare-earth texture" was formed in all three samples. This kind of texture is formed when basal planes are rotated around 45° from the extrusion direction symmetrically around extrusion axis [42]. However, in the N3 and WN43 additional texture element formed in the center of the pole figure, but not in the W3. It could be suspected that this peak in the center of pole figure is an effect of neodymium addition [43].

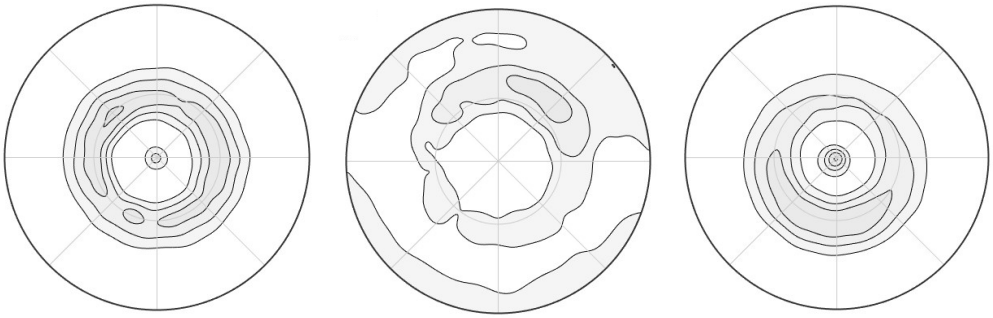

(a) max: 2.6 (b) max: 2.5 (c) max: 2.5

Figure 5.2: (0001) pole figures of the extruded samples a) N3, b) W3 and c) WN43.

Distribution of secondary phase particles in all extruded samples was studied by SEM and results are presented in Figure 5.3. As can be seen in Figure 5.3*a*, the precipitates in the N3 are primarily located at the grain boundaries. They probably precipitated during the extrusion process. On the other hand, such precipitation behaviour was not found in the W3, only small amount of particles that were aligned in stripes along the extrusion direction was observed, see Figure 5.3*b*. Eventually, microstructure of the WN43 presents combination of microstructure of both binary alloys, presented in Figure 5.3*c*. Fine precipitates at the grain boundaries, well seen in Figure 5.3*d*, as well as stripes of the particles were observed. We assume that annealing of the investigated material prior to the extrusion did not lead to complete dissolution of all secondary phase particles. All microstructural characteristics of the extruded samples were published in our paper [44]. Figure 5.3*e* shows representative microstructure of the extruded samples treated by annealing. Almost all secondary phase particles are dissolved; however, only very small particles are observed homogeneously dispersed in the Mg matrix in all three alloys. EDX analysis revealed that these undissolved particles contained except for Mg, Y and Nd also oxygen and iron.

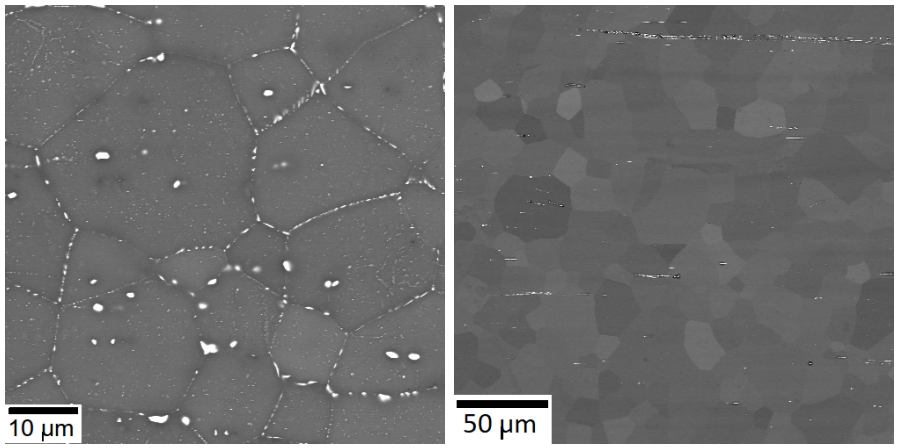

(a)

(b)

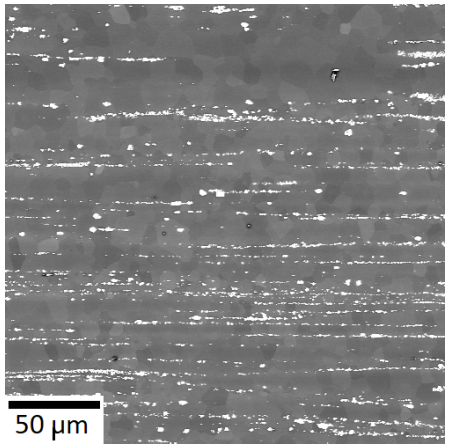

(c)

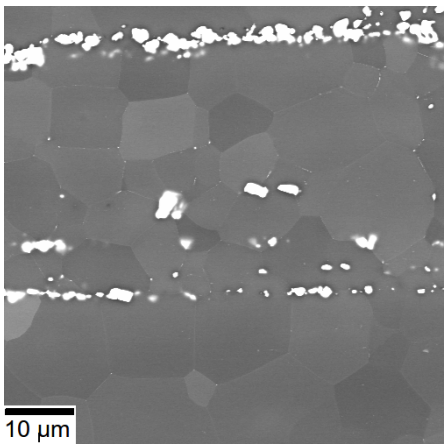

(d)

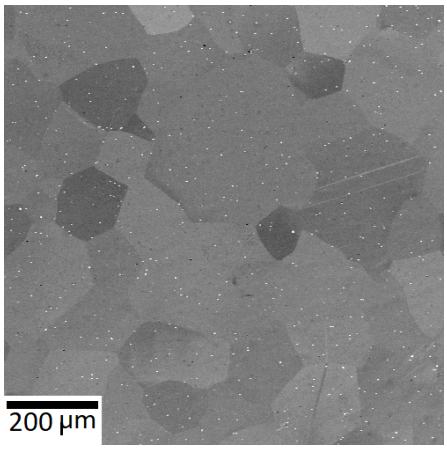

(e)

Figure 5.3: The secondary phase particles distribution of the extruded samples a) N3, b) W3, c) WN43 d) detail of WN43, e) T4-Ex of WN43.

5.2 The microstructure evolution after ECAP

After the extrusion, severe plastic deformation was introduced to all three alloys by ECAP. Our samples passed through the ECAP once (1P), twice (2P), four times (4P) or eight times (8P). The plane of observation was perpendicular to the ECAP pressing direction. The average grain size, distribution of grain size and fraction of low (LAGB) and high angle grain boundaries (HAGB) were calculated from EBSD data as weighted area fraction. The distribution of the secondary phase particles was studied by SEM and chosen states were shown.

5.2.1 N3 alloy

The ECAP processing lead to substantial changes of microstructure of N3 alloy. After first pass (Figure 5.4*a*), the microstructure had duplex structure and contained mainly areas of coarse grains surrounded by small ones with diameter around 2-3 µm. Close inspection of the coarse grains shows that they contain smaller subgrains generally segregated by low angle boundaries. After 2 passes, see Figure 5.4*b*, the microstructure became formed more by equiaxed grains and homogeneous with less evidence for the presence of the coarse grains. Subsequent passes through ECAP resulted in further grain refinement and the new microstructure, mostly with grains smaller that 2 µm, was formed. The corresponding micrograph of 4P is illustrated in Figure 5.4*c*. Introduction of additional strain through 8 passes, see in Figure 5.4*d*, led to the formation of equiaxed grains of uniform distribution with average grain size of 1 µm.

Massive precipitation in the microstructure was observed during the first pass of ECAP processing. Figure 5.5*a* of 1P condition shows that beside particles observed along the grain boundaries severe precipitations occurred especially in large grains. Further processing through ECAP did not lead to change in secondary phase particles distribution. The development of secondary phase particles describes Figure 5.5*b*.

5.2.2 W3 alloy

Microstructure of W3 alloy does not seem to be as bimodal as in the case of N3 alloy after the first pass of ECAP. Dominating grains have diameter ∼5 µm and ∼15 µm. But, regions of more coarse grains are present, as shows Figure 5.6*a*. Second ECAP pass resulted in microstructure with bimodal character of grain size distribution, presented in Figure 5.6*b*. Thus, new refined grains with diameter of 1-2 µm were arranged between the large grains with diameter ∼10 µm. Development of microstructure after fourth pass was very similar to that of the N3 alloy. The microstructure become more refined and areas with coarse grains disappeared, see Figure 5.6*c*. Similarly to the N3 we achieved homogeneous microstructure with equiaxed grains. Average grain in the 8P sample size was ∼600 nm.

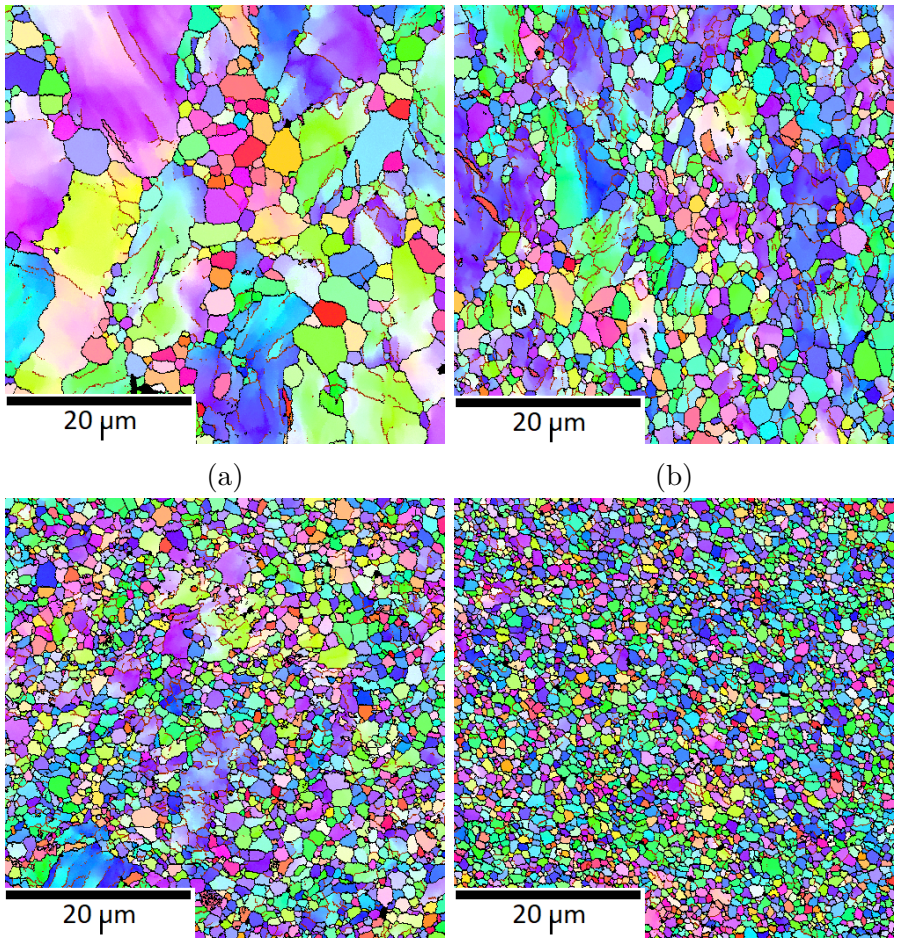

(a) (b)

(c) (d)

Figure 5.4: The EBSD micrographs of N3 alloy a) 1P, b) 2P, c) 4P and d) 8P.

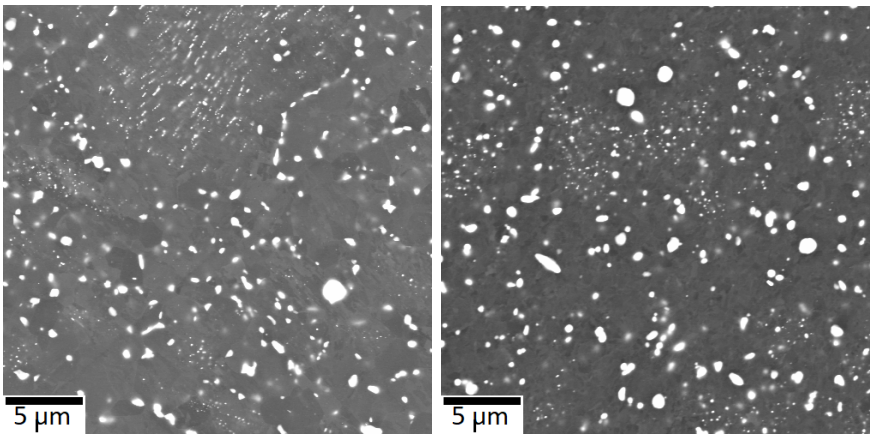

(a) (b)

Figure 5.5: The distribution of secondary phase particles of N3 alloy processed by the ECAP a) 1P, b) 8P.

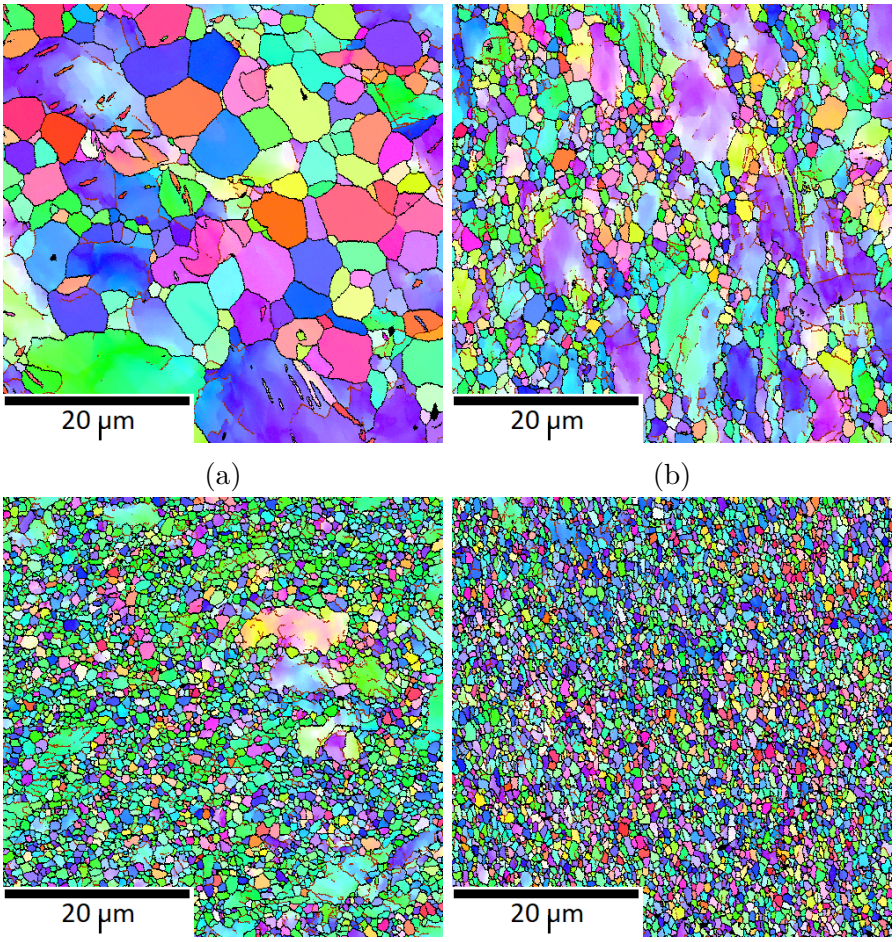

(a) (b)

(c) (d)

Figure 5.6: The EBSD micrographs of W3 alloy a) 1P, b) 2P, c) 4P and d) 8P.

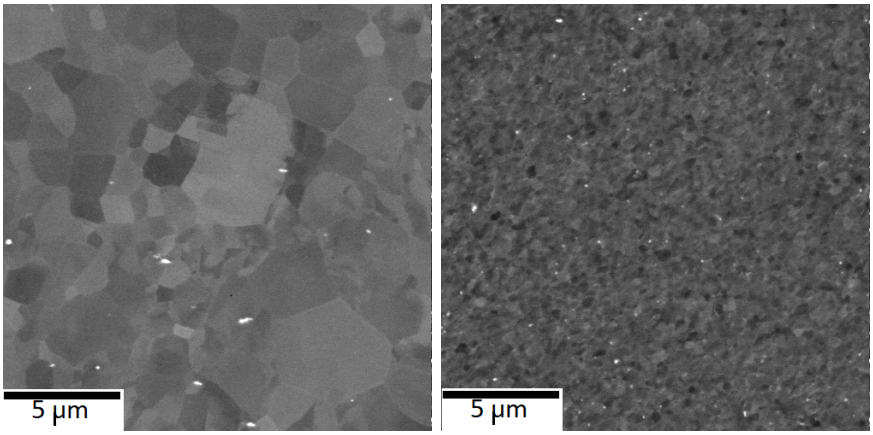

(a) (b)

Figure 5.7: The distribution of secondary phase particles of W3 alloy processed by the ECAP a) 1P, b) 8P.

Development of secondary phase particles between 1P and 8P conditions is described in Figure 5.7*a* and 5.7*b*. In contrast to the N3 alloy, only very small fraction of randomly delocalized secondary phase particles was found in the W3 alloy after one pass of ECAP. The situation did not change after eight ECAP passes.

5.2.3 WN43 alloy

Similarly to the N3 alloy, after the first pass of ECAP the microstructure was highly inhomogeneous and bimodal character of the grain size distribution dominated, as shown in Figure 5.8*a*. Grain size of the small grains was ∼1 µm but the size of larger grains was up to 23 µm in diameter. After the second pass through ECAP duplex character of the grain size distribution still remained, but area fraction of the smaller grains was comparable to the area fraction of the large ones, as shown in Figure 5.8*b*. During subsequent ECAP passes up to 4P, further fragmentation of the coarse grains occurred, resulting in almost homogeneous microstructure. Even though, presence of much bigger grains with size up to 7 µm was still apparent in 4P sample, as shown in Figure 5.8*c*. Finally, the uniform distribution of equiaxed grains with average grain size of ∼600 nm was observed after eight passes of ECAP.

Additionally, the sample of WN43 treated by annealing at temperature 525° for 16 h prior to the ECAP (T4-8P) was also investigated. Almost the same microstructure as for 8P condition was observed in this sample with the slighly higher average grain size of ∼750 nm. The respective micrographs are shown in Figure 5.8*d* and 5.8*e*. These results were already published in paper [45].

The evolution of the secondary phase particles distribution after one and eight passes of ECAP is shown in Figure 5.9. Substantial change of the distribution and size of secondary phase particles was observed. During first pass through ECAP massive precipitation also occurred at the grain boundaries and within grains. This precipitation continued after subsequent ECAP processing. Moreover, during further ECAP processes, large secondary phase particles were subsequently refined and redistributed. Thus, microstructure of 8P condition, see Figure 5.9*c*, shows homogeneously redistributed fine particles with diameter around 200 nm. Interestingly, comparable microstructure of the T4-8P sample and 8P (see Figure 5.3*e*) suggests, that dissolved secondary phases particles (after annealing) precipitated again during ECAP processing and after sufficient number of passes homogeneous microstructure of fine grains was formed.

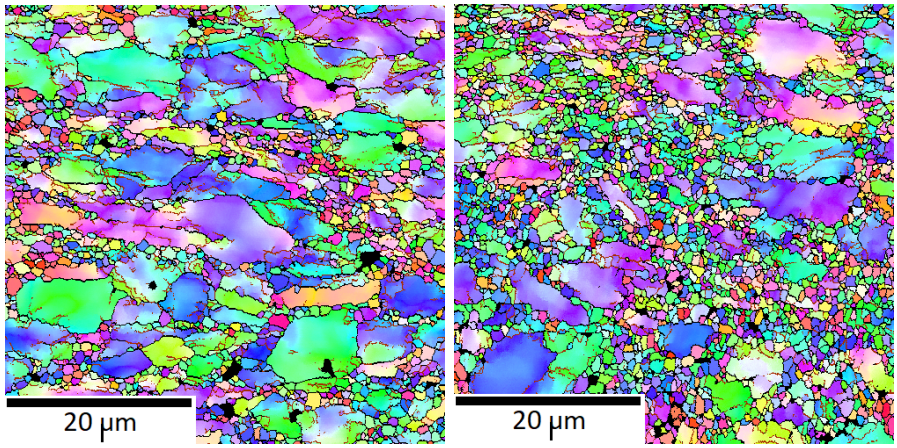

(a)

(b)

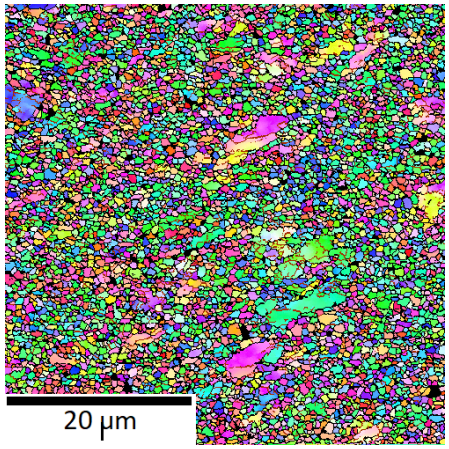

(c)

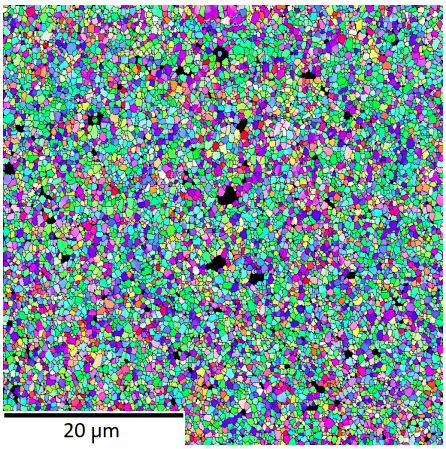

(d)

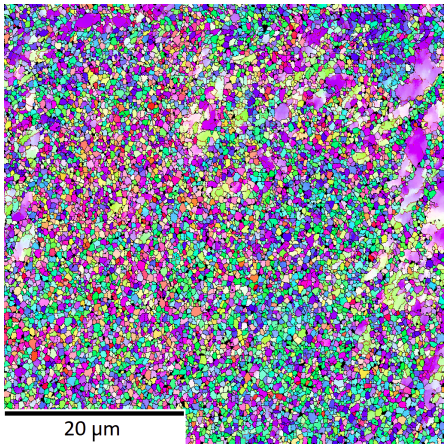

(e)

Figure 5.8: The EBSD micrographs of WN43 alloy a) 1P, b) 2P, c) 4P, d) 8P and e) T4-8P.

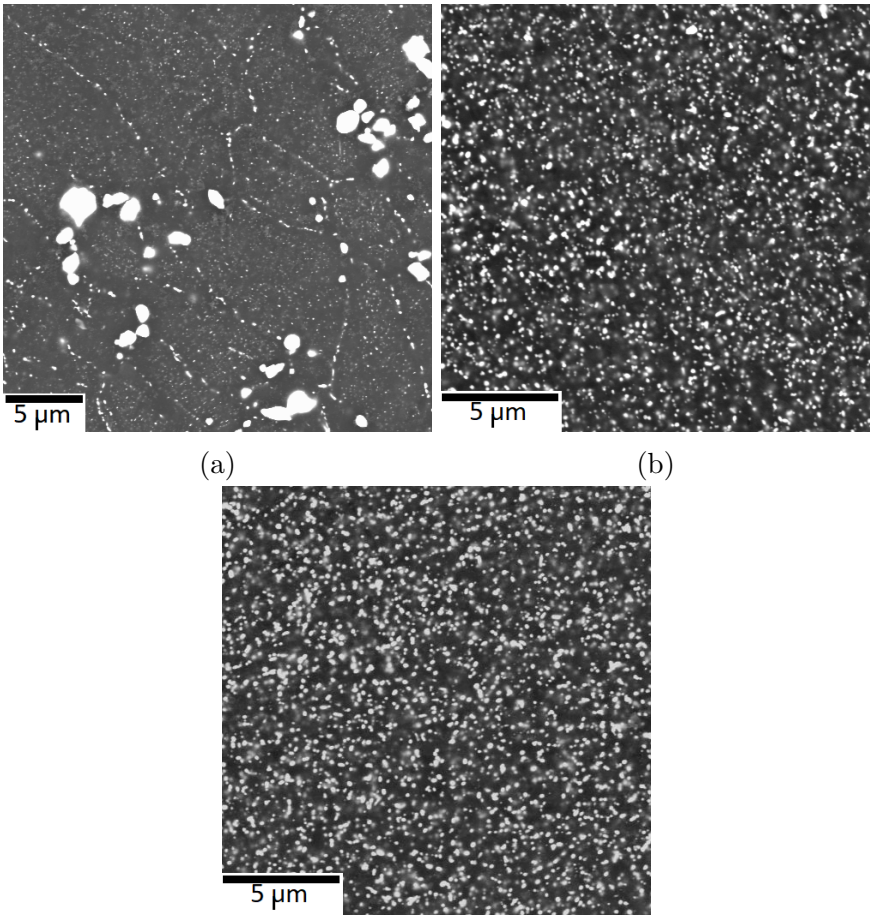

(a) (b)

(c)

Figure 5.9: The distribution of secondary phase particles of WN43 alloy processed by the ECAP a) 1P, b) 8P and c) T4-8P condition.

5.3 TEM observation

In order to acquire deep insight into the microstructure evolution of initial extruded materials and materials processed by the ECAP, TEM observation has been performed. Detailed study of extruded sample of the N3 alloy revealed presence of three types of precipitates. As was mentioned above, most boundaries were decorated with secondary phase particles. According to the TEM, we observed two structural types at grain boundaries. One type of secondary phase particles was identified as FCC (face center cubic) β_1 (Mg_3Nd), shows Figure 5.10*a*. The size of these particles ranges from ∼100 nm to ∼1 µm. The second one was identified as β particle ($Mg_{12}Nd$) tetragonal structural type with a size ∼1 µm, illustrates Figure 5.10*b*. Moreover, another set of intra-granular precipitate was observed and identified as β_e equilibrium intermetallic phase ($Mg_{41}Nd_5$), see Figure 5.10*c*. Further ECAP process lead to a massive precipitation in the N3 alloy. Small particles from boundaries were replaced by spherical ones with size from 500 nm to 1 µm mostly localized at the grain boundaries and triple points, see Figure 5.10*d*. The identification of these particles was not evident but we assume that microstructure included equilibrium β_e particles.

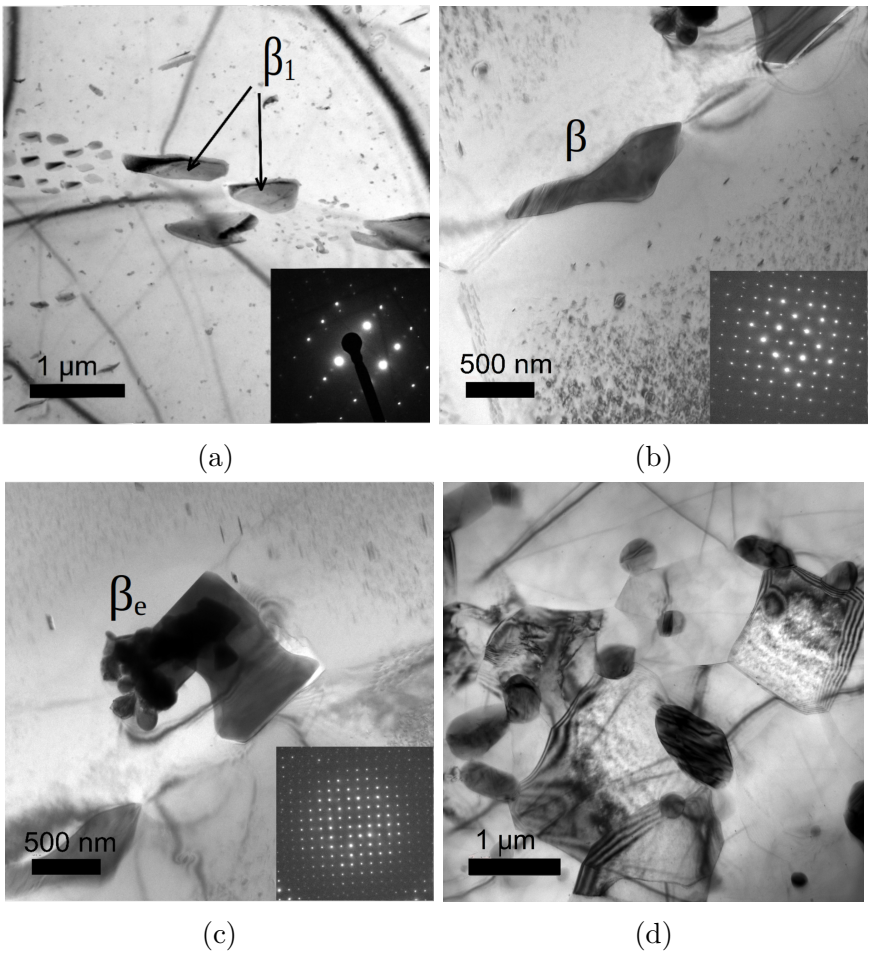

Figure 5.10: TEM images of N3 Ex sample and diffraction patterns of a) β_1, b) β, c) β_e particle, d) N3 8P sample (bright field).

In the case of the W3 small amount of precipitates was observed in both extruded and 8P sample. In both states was found equilibrium β ($Mg_{24}Y_5$) phase, see Figure 5.11*a*. Small spots around particles can be seen in this figure (signed with red cycle), it is probably a contamination from electrochemical polishing of the sample. Figure 5.11*b*, represents microstructure of state after 8 passes of ECAP.

The WN43 showed more complex precipitation evolution. As was seen in SEM results, in extruded state we observed very small particles with size of less than 100 nm at the grain boundaries, see Figure 5.12*a*, and larger ones were mostly localized in groups, see Figure 5.12*b*. After eight passes through ECAP we observed only one type of secondary phase particles mostly found at the grain boundaries and triple points, shown in Figure 5.13. We assume that large precipitates presented after extrusion were subsequently fragmented during ECAP process; moreover, new one precipitated during processing as was described above.

Neverthelles, chemical composition analysis of the particles after extrusion and eight passes through ECAP revealed in both cases presence of yttrium and

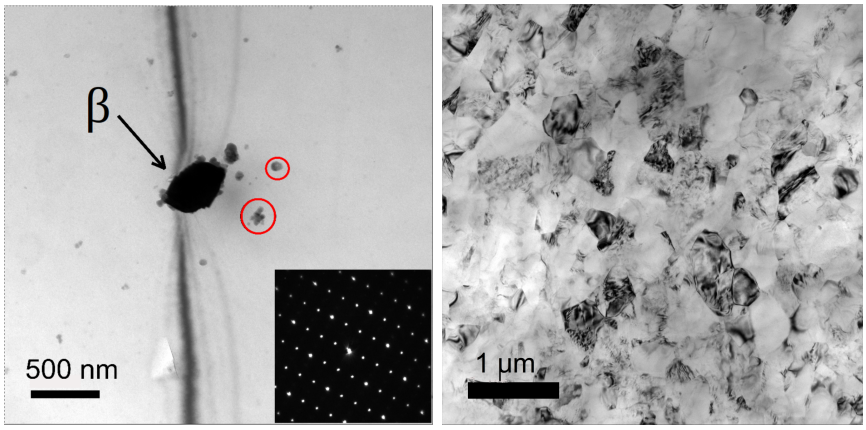

(a) (b)

Figure 5.11: TEM images of W3 a) Ex sample with diffraction pattern of β particle, b) 8P sample (bright field).

neodymium with the varying ratio in different particles. Analyses of diffraction patters did not give a clear evidence of structural characteristics, but we assume that it will be Mg_5RE type structure, consistently with previous reports of the WE43 alloy [46] and [47].

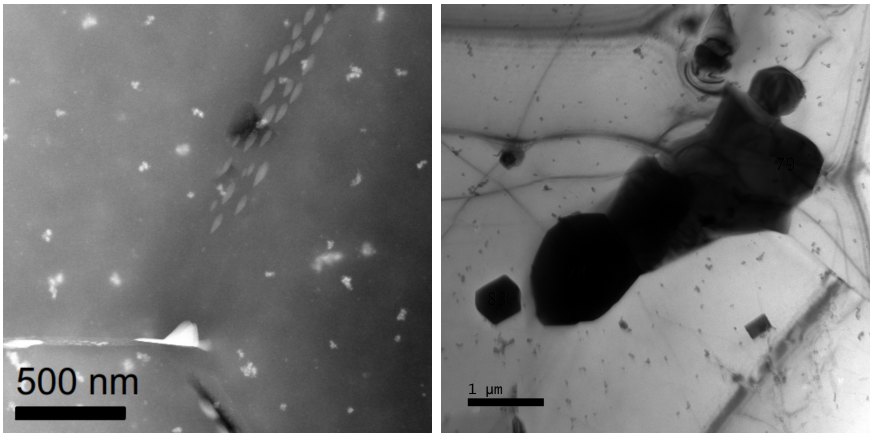

(a) (b)

Figure 5.12: TEM image (bright field) of WN43 a)STEM image of fine precipitates at boundaries of Ex sample, b) cluster of precipitates in Ex sample.

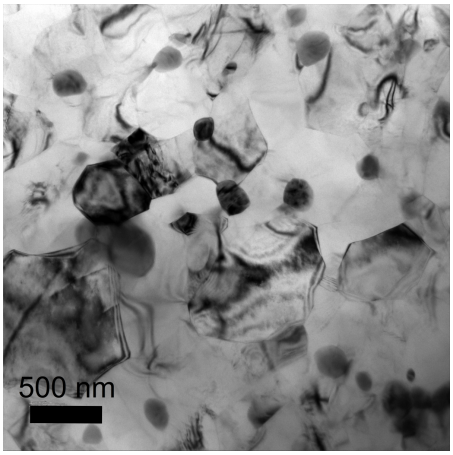

Figure 5.13: TEM image (bright field) of WN43 8P sample.

5.4 Texture evolution after ECAP

Texture evolution after the ECAP pressing was similar in all three alloys. The texture created during extrusion was in all alloys replaced by new texture elements since first pass through ECAP. The texture development of all three alloys is summarized in Table 5.1.

After the first ECAP pass, initial texture corresponding to basal planes oriented ∼45° from the extrusion direction was replaced by new texture where basal planes were almost perpendicular to process direction, as shows Figure 5.1*a*. However, one texture element from the initial texture is still visible. Moreover, the peak from the centre of pole figure created during the extrusion also disappeared. A similar character of the texture was found in 2P sample, as shows Figure 5.1*d*, but grains with basal planes perpendicular to Y axis were not visible anymore. After four passes, most of the grain rotated back and created texture with basal planes almost perpendicular to process direction and 45° texture elements disappeared. After eight passes, the 45° texture element became again dominant and slightly shifted towards the Y axis, as shows Figure 5.1*j*.

The evolution of texture of the W3 and WN43 alloys was very similar to that of the N3 alloy. However, the texture element corresponding to basal planes oriented 45° from process direction became more pronounced since four ECAP passes for the W3 and two passes through ECAP for the WN43 alloy. Moreover, pole figures of 8P and T4-8P samples of the WN43 show similar texture development with slightly higher maximum of intensity in the case of T4-8P visible in Figures 5.1*l* and 5.1*m*, respectively.

It is necessary to mention that in investigated alloys were observed the formation of unusual texture character where basal planes oriented are 45° from process direction. Overall, the texture was in all cases very weak. However, this atypical texture have been already observed and identified in LAE442 [48] and WE43 [46] Mg alloys processed by ECAP.

	N3	W3	WN43
P1	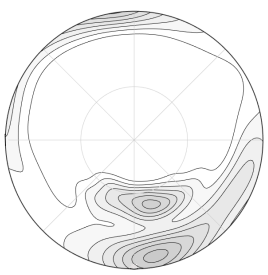 (a) max: 4.7	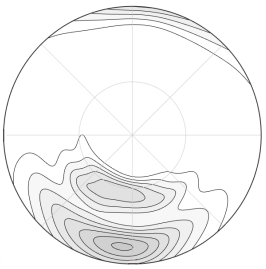 (b) max: 4.6	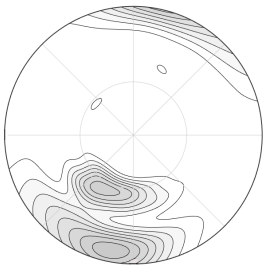 (c) max: 4.9
P2	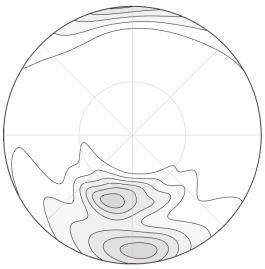 (d) max: 3.8	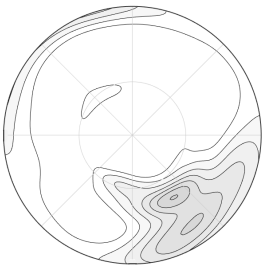 (e) max: 4	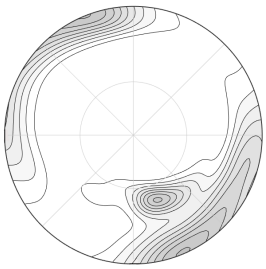 (f) max: 5.1
P4	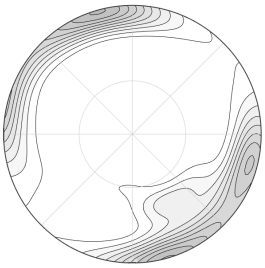 (g) max: 5.6	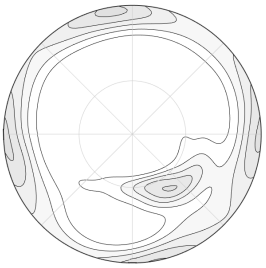 (h) max: 3.1	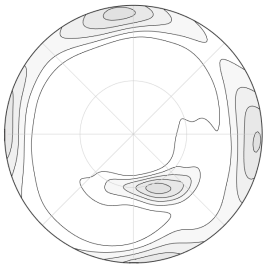 (i) max: 3.3
P8	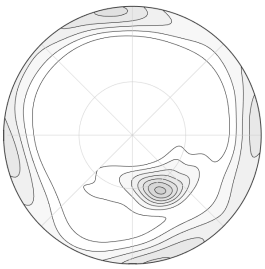 (j) max: 4.2	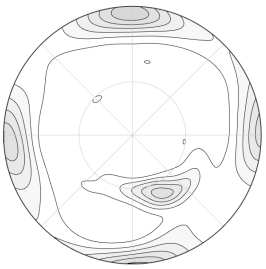 (k) max: 3.9	 (l) max: 2.9
T4-8P			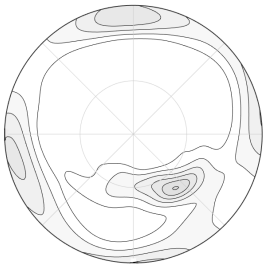 (m) max: 3.5

Table 5.1: (0001) pole figures of N3, W3 and WN43 alloys after ECAP.

5.5 Mechanical properties

Mechanical properties as a function of increasing number of ECAP passes was studied by compression deformation tests and microhardness tests. Compression deformation tests were performed in the directions – along processing direction (X) and transverse direction (Y). These directions were chosen to investigate possible anisotropy of the processed material.

5.5.1 Compression deformation tests

Resulting true stress - true stein curves of extruded samples of the N3 and W3 alloys can be seen in Figures 5.14*a*. Inspection of the deformation curves of the N3 alloy reveals difference in their shape for X and Y in an early stage of the plastic deformation. The same differences were also noticed in extruded condition of the WN43, but were not so obvious as in the case of the N3. However, no difference in the shape of the deformation curves of the W3 alloy was observed. The true stress - true stein curves determined in the WN43 material processed by 1 and 8 passes of ECAP are also shown for comparison in Figure 5.14*b*. We observed differences in yield stress (better seen in Tables 5.2 and 5.3.), but no significant differences in maximum stress, depending on the compression direction. A notable plateau right above the yield point is visible in both 8P samples, overall a sharp yield point is seen in the deformation curve of 8P sample in X direction. In the case of the other two alloys the character of the deformation curves was similar.

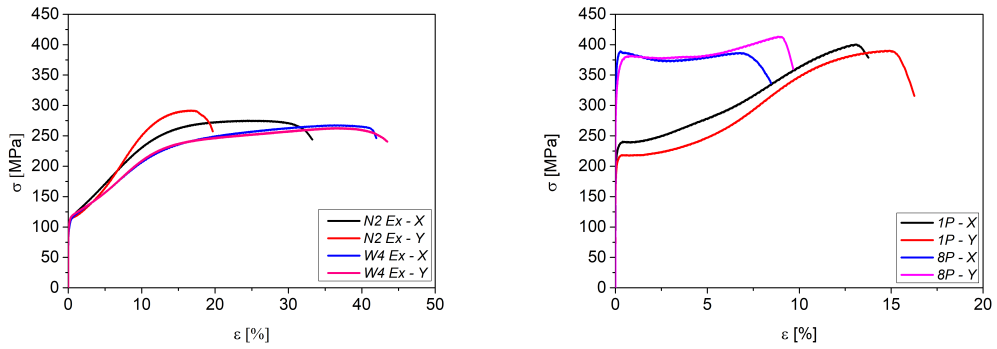

(a) (b)

Figure 5.14: The deformation curves in both directions of a)extruded N3 and W3, b)WN43 after 1 and 8 passes through ECAP.

For each alloy and each condition, the yield compression strength (YCS) at 0.2% strain offset and ultimate compression strength (UCS) were evaluated from compression tests and are presented in Figure 5.15 and in Tables 5.2 and 5.3.

In the case of extruded N3 and W3, values of YCS were similar in both directions. By contrast, extruded condition of the WN43 exhibits opposite relation, thus higher YCS was observed in the Y direction compared to the X direction. Processing through the ECAP exhibits excellent mechanical properties for both directions. After eight passes of ECAP, YCS of all investigated materials significantly increased above ∼300%. Generally, the evolution of yield strength of all

three alloys was similar and thus strength increased significantly with the increasing number of ECAP passes. It is obvious that the WN43 reached the highest strength for all of ECAP conditions and the N3 alloy the lowest. Moreover, considerable increase of YCS was observed in both deformed directions. However, the YCS in the X direction was slightly higher or at least similar within statistical error for all studied states compared to Y direction. The evolution of the ultimate compression strength had also increasing tendency as a function of ECAP passes and correlated with the evolution of YCS for both directions.

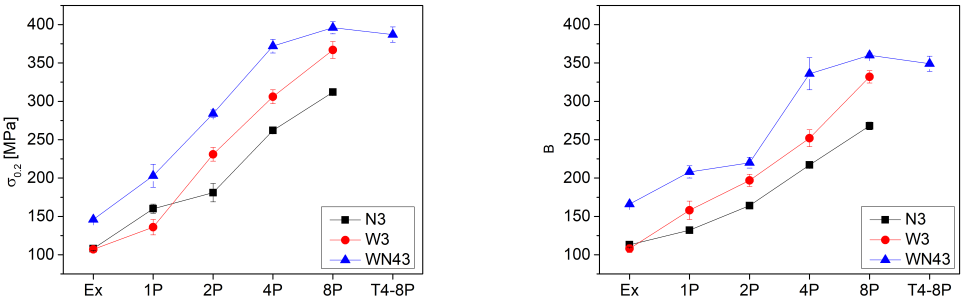

(a) (b)

Figure 5.15: The svolution of yield compression strength as a function of the increasing number of ECAP passes for a) X direction and b) Y direction.

	$\sigma_{0.2}$ - X			σ_{max} - X		
	N3	**W3**	**WN43**	**N3**	**W3**	**WN43**
Ex	108 ± 2	107 ± 3	146 ± 2	274 ± 5	264 ± 5	340 ±5
1P	160 ± 6	136 ± 10	203 ± 15	315 ± 27	310 ± 4	352 ± 18
2P	181 ± 12	231 ± 9	284 ± 5	316 ± 22	350 ± 9	430 ± 46
4P	262 ± 3	306 ± 9	372 ± 9	366 ± 22	356 ± 12	421 ± 18
8P	312 ± 3	367 ± 11	396 ± 8	384 ± 11	445 ± 8	393 ± 8
T4-8P	-	-	387 ± 10	-	-	404 ± 13

Table 5.2: Yield compression strength and ultimate compression strength measured in the X-direction.

	$\sigma_{0.2}$ - Y			σ_{max} - Y		
	N3	**W3**	**WN43**	**N3**	**W3**	**WN43**
Ex	113 ± 3	108 ± 5	16 6± 2	290 ± 2	258 ± 12	333 ± 2
1P	132 ± 4	15 8± 12	208 ± 8	330 ± 12	325 ± 16	382 ± 15
2P	164 ± 3	197 ± 8	220 ± 7	314 ± 8	35 7± 12	496 ± 15
4P	217 ± 4	252 ± 11	336 ± 21	346 ± 13	382 ± 12	42 1± 15
8P	268 ± 5	332 ± 8	360 ± 3	368 ± 4	432 ± 12	417 ± 11
T4-8P	-	-	34 9± 10	-	-	420 ± 7

Table 5.3: Yield compression strength and ultimate compression strength measured in the Y-direction.

5.5.2 Microhardness tests

Microhardness tests were carried out to investigate homogeneity of mechanical properties. The tests were measured on a plane perpendicular to the process direction. The results showed a homogeneous distribution of the microhardness in the cross-section of all investigated conditions. Average values of the microhardness as a function of ECAP passes are presented in Figure 5.16 and Table 5.4. In general, ECAP causes significant increase in microhadrness. As illustrates Figure 5.16, the microhardness of the WN43 is higher than the W3 and N3 for all conditions and the N3 has the lowest values of microhardnes. These results correlate well with previous results of the mechanical properties.

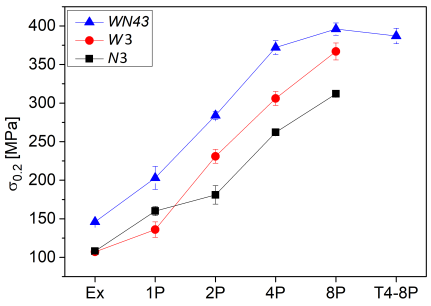

Figure 5.16: The microhardness of all investigated alloys as a function of the increasing number of ECAP passes.

$HV_{0.1}$ (Vickers 0.1)			
	N3	**W3**	**WN43**
Ex	56 ± 2	57 ± 3	74 ± 2
1P	60 ± 3	63 ± 2	83 ± 2
2P	68 ± 3	76 ± 2	90 ± 2
4P	75 ± 2	87 ± 3	99 ± 2
8P	82 ± 3	100 ± 3	105 ± 4
T4-8P	-	-	107 ± 3

Table 5.4: The microhardness of all investigated alloys.

5.6 Linear polarization tests

Corrosion behaviour of all three investigated alloys was studied by linear polarization tests. The tests were conducted in 0.1M NaCl solution at the room temperature. This measurement method is particularly useful for an estimation of initial corrosion attack.

After 10 minutes of stabilization, the linear polarization curves were measured and are shown as Evans diagrams in Figure 5.17. No variations of curve shapes in the electrochemical response between the extrusion samples and other samples processed through ECAP were observed. But, samples of the N3 alloy revealed subsequent shifting of the corrosion potential E_{corr} to the more noble values after ECAP. On the other hand, opposite effect was observed for the W3 samples and almost no differences were found in corrosion potential of the WN43 alloy. Interestingly, annealing treatment of the extruded samples caused a significant shift of E_{corr} towards more negative values for all three alloys. The same shifting towards negative values was observed also for the T4-8P sample.

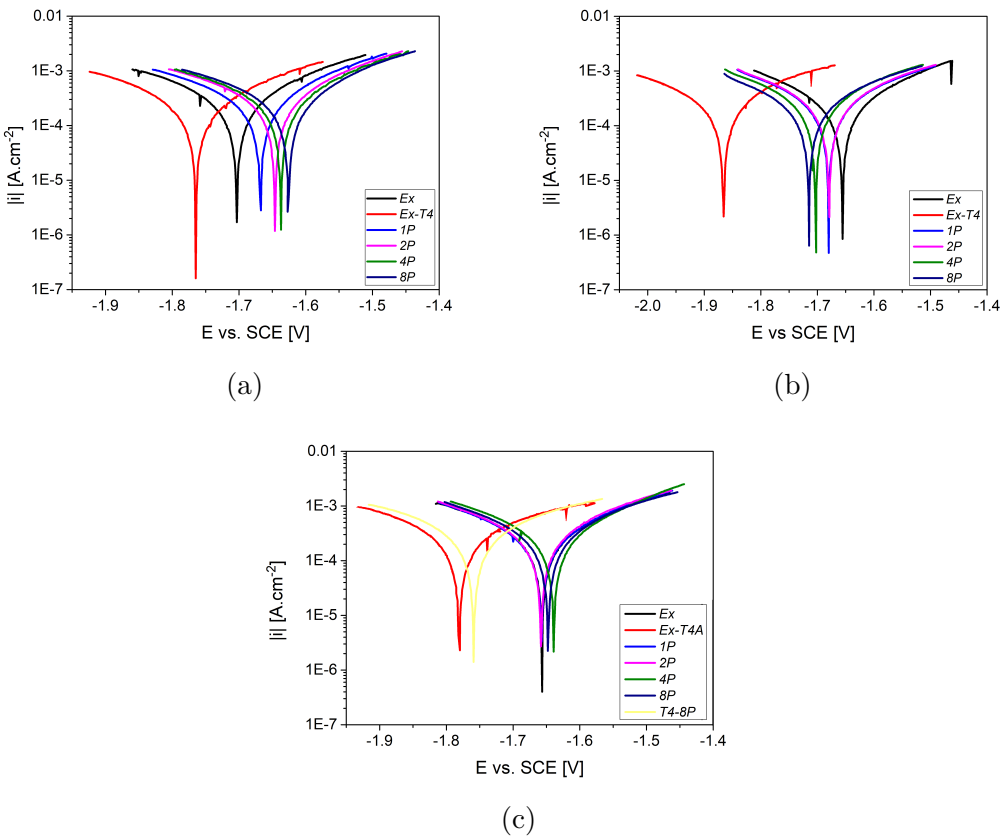

Figure 5.17: Th Evans diagrams of the investigated alloys a) N3, b) W3, c) WN43.

Polarization resistance (R_p) was estimated from the polarizations curves. The resulting values of the R_p for all alloys and their conditions are presented in Table 5.5 and graphically illustrated in Figure 5.18. As can be seen, the evolution of the polarization resistance of the N3 and WN43 is almost similar, furthermore, their evolutions have decreasing tendency with increasing number of ECAP passes. On

the other hand, polarization resistance of the W3 continuously increases with subsequent ECAP processing. Additionally, extra samples Ex-T4 were also studied in order to examine the influence of the alloying elements on the corrosion properties. These samples showed different development of initial corrosion resistance in all cases. For the WN43 is value of R_p in Ex-T4 slightly lower than for Ex condition. In the case of the W3 are values of R_p similar within statistic error, but Ex-T4 of the N3 alloy exhibit the highest value of polarization resistance compared to the other conditions.

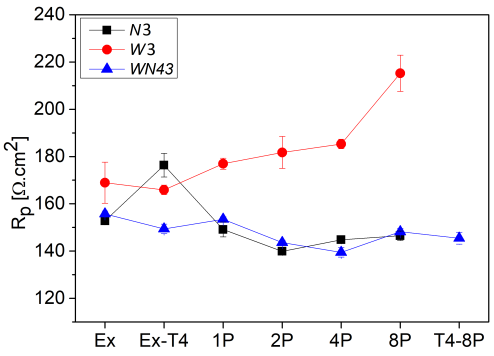

Figure 5.18: The polarization resistance of all investigated alloys as a function of the increasing number of ECAP passes.

	R_p [$\Omega.cm^2$]		
	N3	**W3**	**WN43**
Ex	153 ± 2	169 ± 9	156 ± 2
Ex-T4	176 ± 5	165 ± 2	149 ± 2
1P	149 ± 3	177 ± 2	153 ± 2
2P	140 ± 2	182 ± 7	144 ± 2
4P	145 ± 2	185 ± 2	139 ± 2
8P	146 ± 2	215 ± 8	148 ± 2
T4-8P	-	-	145 ± 3

Table 5.5: The polarization resistance of all investigated alloys.

6. Discussion

In the previous chapter, detailed characterization of microstructure evolution, compression deformation tests and corrosion resistance were presented. Thermomechanical processing such as extrusion and ECAP are forming processes which introduce in the material large plastic strain and noticeably affect the microstructure and thus also other material properties. Result of these deformation processes is, however, dependent on processing parameter, such as processing temperature, type/number of passes, pressing rate and die geometry. There are many papers presenting results in this field on various materials, including magnesium alloys [24], [32], [33]. Here is discussion of important topics of my research.

6.1 The microstructure evolution

The microstructure of the N3 and WN43 alloys was fully recrystallized after the extrusion with a uniform character of a grain size. Unfortunatelly, the W3 alloy exhibits formation of prolonged grains in the extrusion direction, but most of grains are also recrystallized and uniform. Contrary to the substantially higher amount of the alloying element in the W3 compared to the N3 alloy, grain refinement was more intensive in the latter one. This difference stems from different distribution of the precipitates in the matrix [44]. As illustrates Figure 5.3 of distribution of secondary phase particles after the extrusion, precipitates in N3 are primarily situated at the grain boundaries, thus they stabilise the grain structure and prevent grain growth. In case of the W3 such precipitates were not found, only small amount of the secondary phase particles, that are aligned in stripes along the extrusion direction. The microstructure of the WN43 presents combination of these two binary alloys, with the difference, that fraction of undissolved secondary phase particles was considerably higher. We can assume that these large particles were presented in microstructure before extrusion, and thus the temperature of homogenisation annealing treatment before extrusion was not high enough for dissolution of all secondary phase particles.

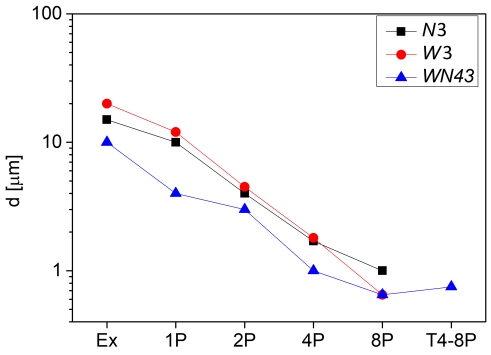

Figure 6.1: The evolution of the average grain size with the increasing number of ECAP passes.

ECAP processing resulted in a significant decrease of average grain size with fraction of high angle grain boundaries in all three alloys. The degree of grain refinement and grain structure homogeneity is proportional to the number of ECAP passes [11]. Resulting evolution of average grain size of all three alloys is presented in Figure 6.1. The refinement in the grain structure was the most significant in the WN43 and W3 alloy, in which average grain size achieved 600-700 nm after 8 passes. Despite the fact, that similarly as after extrusion the N3 alloy contained considerably higher amount of precipitates, grain refinement during ECAP was much severe in the W3 alloy. In the case of the N3, the final average grain size was ∼1 µm after 8 passes. This corelates with results of nucleation and precipitation processes in Mg-Al-Y ternary systems, where Y leads to a very satisfying grain refinement similar to the popular zinc [49].

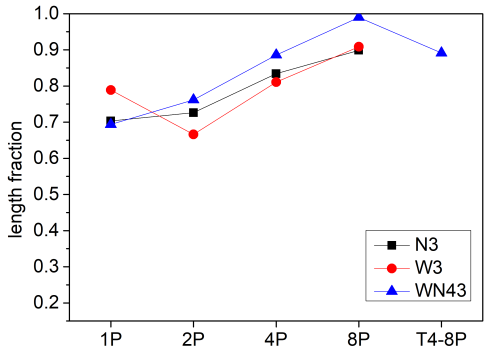

Figure 6.2: The evolution of the average grain size on the increasing number of ECAP passes.

The HAGB and LAGB are described as boundaries with disorientation greater than 15° and less than 15°, respectively. Both the HAGB and LAGB are complementary to each other. Thus, evolution of the HAGB is presented in Figure 6.2 for all three alloys processed through ECAP. All alloys exhibit high length of the HAGB since first pass through ECAP and continuous processing resulted in increase of the length of HAGB. The high length fraction of HAGB suggests a high degree of recrystallization since the first pass.

Despite different initial condition before ECAP processing, the final microstructure of the T4-8P exhibits similar average grain size and also similar distribution of secondary phase particles as the 8P condition. Thus, precipitation process and redistribution of them must be present during ECAP pressing. And therefore, it is necessary to say, that in case of WN43 the final microstructure after ECAP does not depend on the initial microstructure.

From the Figure 5.9 can be assumed that ECAP can effectively refine not only grains but also can generate homogeneous distribution of secondary phase particles [34], due to the high strain inserted into the material. Refinement of the secondary phase particles was gradual process and required more than 4 passes of ECAP. We assume that ECAP process also led to the formation of new stable secondary phase particles observed in the TEM images of 8P conditions of the

N3 and WN43 alloys.

Repetitive processing by ECAP led to the development of similar texture in all studied alloys. After eight passes through ECAP the typical texture illustrated in Figure 6.3 was represented by four maxima marked as ”1” and ”2” and additionally by a texture element marked as ”3”. First component corresponded to basal planes almost parallel to the processing direction and almost perpendicular to Z axis. Second component corresponded also to basal planes parallel to the processing direction but almost perpendicular to Y axis. The third one was created by basal planes rotated by 45 ° from the processing direction. Formation of a texture element marked as 3 was observed previously in other magnesium alloys processed by ECAP [48], [50]. According to paper [48], this texture element was a result of the activity of the basal slip systems causes rotation of the basal planes parallel to the geometric slip plane of ECAP. This texture element became dominant in the early stage of ECAP process in alloys with higher amount of the alloying RE elements. Thus, it suggests that higher content of RE elements can promote formation of this texture element since first ECAP pass. The formation of the first two components was caused by the plastic deformation with activity of the non-basal slip systems, also reported in [48]. The activation of the non-basal slip was probably attribute of elevated temperature during ECAP processing [51] and alloying elements.

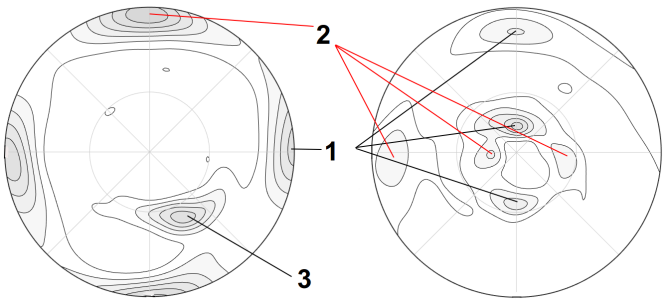

Figure 6.3: The pole figure of the W3 8P sample a) (0001) b) $(10\bar{1}0)$.

6.2 The mechanical properties

Compression deformation tests were performed in the two perpendicular directions: X and Y, in order to investigate the potential anisotropy resulting from the thermomechanical processing.

After the extrusion, the values of YCS for the N3 and W3 were similar regardless of the different grain size and different amount of the intermetallic phases. Additionaly, differences of strength according to different compression directions were not found. The explanation of the similar values of YCS can be found in the different strengthening factors. Thus, in the case of the W3 solute solution strengthening balances negative effect of higher average grain size and lower amount of intermetalic phases compared to the N3. In the case of the WN43, the lowest grain size together with precipitation strengthening resulted in the

highest strength in both directions compared to other binary alloys. However, the higher mechanical strength was measured in the Y direction. This difference could be explained by a higher number of particles aligned in the stripes along the extrusion direction [44]. Moreover, difference in a shape of the the deformation curves of the N3 and WN43 was observed, but not for the W3 alloy. From the Figure 5.14*a* can be seen that sample deformed in the Y direction has evidently S-shape character of the curve. It is well known that such a shape of deformation curve is a result of twinning activity [29]. Details of pole figures of the extruded samples help us to identified different mechanisms during different deformation directions. From Figure 6.4*a* are evident two preferred orientations of grains of the N3 alloy. The first is component created by basal planes rotated ∼45° symmetrically around the extrusion direction. This component is similar also for the W3 alloy. The second one, in the middle of the pole figure, is created by basal planes perpendicular to the extrusion direction and is unique. The most common tensile twins are activated in Mg when load is applied perpendicular to the c-axis [29]. Thus, first component contains grains well oriented for basal slip in both directions, so these grains do not affect the shape of the curve. Nevertheless, in case of a deformation in the Y direction the situation is more complex. The orientation for twinning activity are illustrated well in Figure 6.4*b*. So, in the Y direction higher number of grains can twin, which correlates with bolder S-shape of deformation curve in the Y direction. Overall, the higher twinning activity in Y direction was also proved by EBSD micrographs (Figure 6.5) which were measured after pre-deformation to 3% deformation strain. In those micrographs can be seen that length of twin boundaries (red lines) is twice longer in Y direction that in X direction.

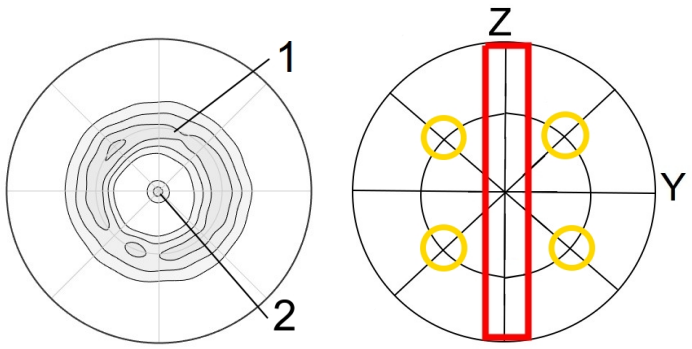

Figure 6.4: a) Pole figure (0001) of extruded N3 alloy, b) texture elements preferable for twinning (red area) and for basal slip (yellow area) in Y direction.

It should be noted that the origin of the texture that occurred only in the N3 and WN43 revealed that it is closely related to the presence of neodymium. This kind of texture component was also reported in magnesium alloy with 1% of Nd processed by extrusion [43]. However, the existance of this component strongly correlated with temperature and speed of extrusion. Overall, all extruded textures were very weak and the fraction of the grains represented by this texture is low. The weakening the of texture is one of the attributes of rare earth elements [52].

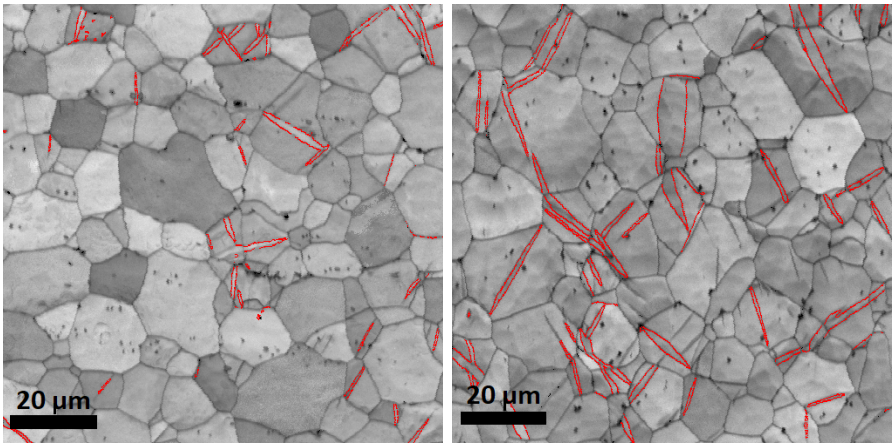

(a) (b)

Figure 6.5: Twin boundaries visible in a) X and b) Y direction.

The results after ECAP showed excellent mechanical properties for both compression directions. The strength of all investigated conditions increased with increasing number of ECAP passes as a results of gradual grain refinement. The strength that was measured in 8P samples increased more than 3 times compared to the corresponding extruded conditions. Such an increase of strength after ECAP is competitive to similarly processed magnesium alloys [46]. Generaly, ECAP lead to formation soft texture with dominant texture element ”3” thus, many magnesium alloys processed by ECAP exhibits dicreasing of strength [48]. However, presence of the RE elements support formation unusual texture which affected strength of investigated alloys. Moreover, different amount of the RE contained in the alloys had also influence on strength. Obviously, the highest strength in all ECAPed conditions exhibits the WN43 alloy because of the highest rate of grain refinement as well as because of the highest fraction of the secondary phase particles, which were homogeneously redistributed after the ECAP pressing. A slightly lower YCS than WN43 exhibits the W3 alloy, but higher compared to the N3 alloy, despite the fact that the N3 presented higher fraction of precipitates. The smaller amount of precipitates observed in the W3 was balanced by higher rate of grain refinement and solute solution hardening. Abnormal solid solution strengthening effect of Y was also reported in [53]. Only in one condition of the N3 the YCS was higher, due to the lower average grain size in 1P sample.

Comparing values of YCS in the X and Y directions shows that strength in all three alloys is lower in Y direction. Because the ECAP leads to formation microstructure with equiaxed grains and homogeneous distribution of particles, no differences should had been observed anymore. However, texture evolution demonstrates that most of the grains are preferentially oriented so that c-axis is perpendicular to the processing direction. These grains are well oriented for twinning in both X and Y directions, which very well correlates with S-shape character of deformation curves, shown in Figure 5.14*b*. However, this affected plastic deformation. Given that the investigated alloy exhibits very weak textures after ECAP, basal slip should be the dominant deformation mechanism irrespective

of the compression direction [54]. For a better understanding of the differences between values of YCS measured in the X and Y direction, Schmid factor for basal slip systems was calculated. Distribution of Schmid factor for basal slip system for compression in both directions shows Figure 6.6. The distribution of Schmid factor is comparable in both directions but softer orientation with Schmid factor close to 0.5 was slightly higher in the Y direction and harder orientation with lower Schmid factor in the X direction. Because the lower Schmid factor indicates harder activation of basal slip during deformation [48], it explains well higher strength measured in the X direction.

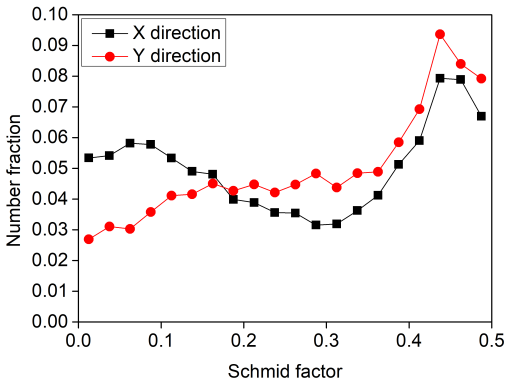

Figure 6.6: The distribution of the Schmid factor in WN43 8P for basal slip system $(0001)\langle 11\bar{2}0\rangle$.

The microhardness test provides another point of view to the mechanical properties of the investigated alloys. It was performed to obtain an information about the homogeneity of the mechanical properties on the cross-section of all studied samples. The results show a homogeneous distribution of the microhardness in the whole studied area and under all conditions. In general, the ECAP causes an accentuated increase in an alloy microhardness as a result of microstructural evolution [48].

Measured values of microhardness with average grain size obtained from EBSD data allows us to determined the validity of Hall-Petch relation presented in Equation (6.1):

$$HV = H_0 + \frac{k}{\sqrt{d}}, \tag{6.1}$$

where H_0 and k are material constant which are obtained from linear regression. HV is the measured value of the microhardness and d average grain size. Figure 6.7 shows the linear regression of the Hall-Petch relation for all three alloys. One can say that the N3 and WN43 alloys are in good agreement with the Hall-Petch relation. Thus, the increase of hardness was affected primaly by grain boundary strengthening in these two alloys. Moreover, the values of fitted parameter H_0 and k are compared to those reported in Mg alloy [55]. In the W3 the linear fit of microhardness data partially fails. Therefore, we included into the Figure 6.7 a line (dashed) with an average of the N3 and WN43 fit. According to this line Hall-Petch relation is in good agreement with till 4 passes through ECAP.

Thus, till first two passes through ECAP was microhardness affected mainly by grain boundary strengthening and after four passes by other strengthening mechanism. According to Figure 5.11*b*, we assume that main strengthening factor was probably higher dislocation density.

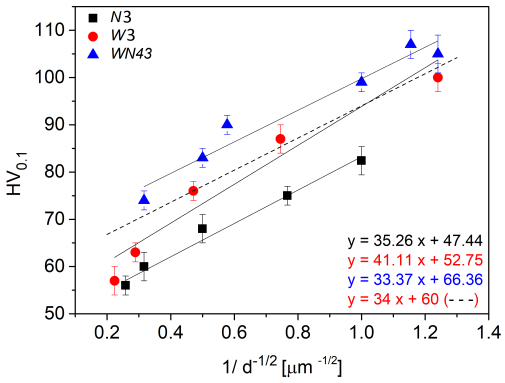

Figure 6.7: The Hall-Petch relationship for the N3, W3 and WN43 alloys based on $HV_{0.1}$ microhardness data.

6.3 Corrosion resistance

Corrosion resistance of the investigated alloys was measured by linear polarization tests to obtain an information about initial corrosion attack. The influence of the thermomechanical processing on corrosion resistance of binary alloy W3 was observed, but no significant influence in the case of the N3 and WN43 was discovered.

As can be seen from Figure 5.17, Evans diagrams measured after 10 minute of stabilization show similar character of the plots for almost all studied conditions. However, results of the N3 alloy revealed subsequent shifting of corrosion potential to lower values with subsequent increase of the ECAP passes. The opposite effect was observed for alloy W3. No shifting of E_{corr} was observed for alloy WN43. Moreover, shifting of E_{corr} to negative values after annealing treatment also do not agree with recent research [56]. According to this paper, dossilution of Y into the Mg matrix had possitive influence on a development of the E_{corr}. Magnitude of the corrosion potential defines a thermodynamic characteristic of the materials and places them to a series according to their relative 'nobility' [57]. Thus, the more negative the E_{corr} is, the high tendency to corrode the material has and vice versa. What we observed is that the material with more noble E_{corr} had lower corrosion resistance and those with less noble E_{corr} had higher R_p. This correlation was not expected and reveals that understanding of structure-corrosion relationships is not at all intuitive and more deeper investigation is needed.

The corrosion resistance of Mg depends on many external or internal factors. It is well known that the corrosion behaviour of Mg alloys is influenced by grain

refinement which leads to changes in density and distribution of grain boundaries. Because the grain boundaries are defects of crystallographic lattice they can promote early corrosion attack. However, existing literature is often contradictory, even within the same alloy class. In paper [58] on a corrosion behaviour of Mg-Zn-Y alloys authors indicate that a decrease of the grain size retarded an occurrence of filiform corrosion and enhanced corrosion properties. However, another studies reported that the corrosion resistance deteriorates as the grain size decreases [34] [59]. Similarly, second phase particles are considered to be helpful for passivation and creation of corrosion products. On the other hand, they can act as galvanic cathode due to the different electrochamical potential beween the matrix and an accelerate the corrosion attack. The particles can form an effective corrosion barrier when the distribution is homogenous and contains fine particles [59]. Nevertheless, particles, such as $Mg_{24}Y_5$ or $Mg_{12}Nd$, that were also observed in our material, had usually higher corrosion potentials than α-Mg matrix and thus were identified as the one that lead to an acceleration of corrosion during initial corrosion attack in WE43 alloys [60]. It should be also pointed out that impurities such as iron, nickel, copper may be present in alloys and significantly accelerate corrosion even at concentrations less than 0.2% [61] because of their low solid-solubility and their abilitys to serve as an active cathodic promoter [62].

Our results of linear polarization tests in extruded samples show similar values of polarization resistance in all three alloys. However, the W3 alloy exhibits slightly higher value of R_p. This is a result of different distribution and fraction of secondary phase particles after the extrusion. In the case of the N3, particles preferably localized at the grain boundaries caused micro galvanic interaction between Mg matrix and negatively influenced corrosion resistance. The same conclusion can be made also for the WN43 that contains mostly large particles aligned in stripes. By contrast, in the W3 only small fraction of the particles was found compared to the N3 and WN43.

Suprisingly, the situation became different after heat treatment. The WN43 exhibited slight decrease of the polarization resistance on the other hand the N3 exhibited significantly higher R_p compared to the extruded sample. In the case of the W3, R_p of both Ex and Ex-T4 was the same within the statistic range. It is necessary to note that after the annealing at 525 °C for 16 h all three samples contained small fraction of fine undissolved secondary phase particles. EDX analysis revealed that these particles included relatively high amount of iron. The characteristic spectrum of such particles can be seen in Figure 6.8. Overall, from the composition of the alloys, see Table 4.1, is apparent that contamination by iron is not negligible. Thus, iron contamination probably caused the enhancing of the corrosion resistance in the WN43, because the alloy contained higher fraction of these particles compared to both binary alloys. The microstructure of the W3 did not change significantly after annealing. Thus, amount of precipitation was in both samples very low. Only size of the grains changed but we assume that this had no noticeable effect and the Y dissolved in Mg matrix had the same protective function. In the case of the N3, we assume that the higher fraction of precipitates at grain boundaries presented after the extrusion had superior acceleration effect on the initial corrosion compared to the smaller fraction of particles

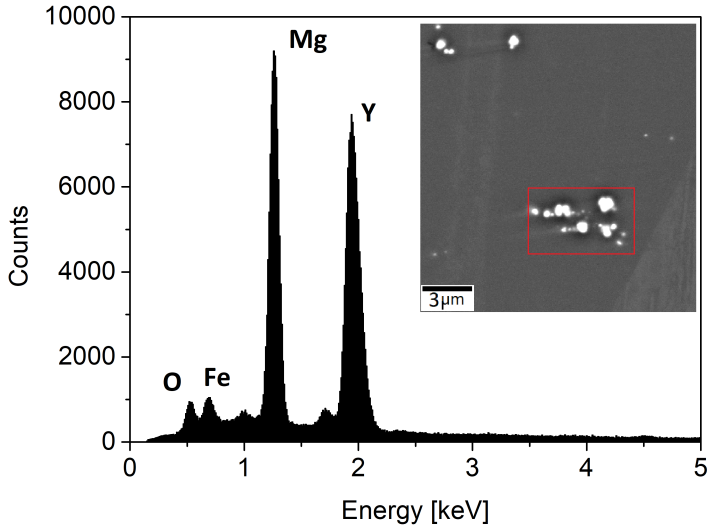

Figure 6.8: The spectrum of the main elements presented in the selected area of WN43 alloy.

available after the annealing.

Further ECAP pressing led to a substantial grain refinement in all investigated alloys together with a substantial redistribution of the secondary phase particles. This had almost no or slightly decreasing effect on the corrosion resistance of the N3 and WN43 alloys. On the other hand, in W3 alloy the increase of R_p was significant. Because the WN43 and N3 contain comparably higher fraction of secondary phases than the W3 alloy, we assume that presence of these particles led to microgalvanic corrosion between particles and Mg-matrix and deteriorated initial corrosion resistance of the WN43 and N3 alloys. In the case of W3, the overall corrosion was probably stifled by the grain refinement.

The corrosion of magnesium alloys is highly complex problem. It depends on several different factors and there is still no one compact theory. The linear polarization test is suitable method to obtain information about the initial corrosion attack, but sometimes not suitable enough and more deeper investigation is needed for the right interpretation of results.

Conclusion

In the present work, three magnesium alloys with different content of neodymium and/or yttrium were studied as potential materials for biodegradable applications in medicine. The work is focused on the influence of two thermomechanical processes: hot extrusion and equal channel angular pressing on the processed materials. Complex microstructural characterization, mechanical properties and corrosion resistance were carried out and these main results can be summarized as follows:

- Generally, homogeneous microstructure with high fraction of high angle grain boundaries was attained after eight ECAP passes. Significant grain refinement was found in all three alloys due to the processing through ECAP. Ultrafine grained microstructure was achieved in W3 and WN43 alloys.

  Final microstructure of WN43 processed through the ECAP did not depend on the initial history of the processed material.

  We observed weak texture development during thermomechanical processing. After the extrusion of N3 and WN43 a unique texture element was observed in the centre of the pole figure. ECAP led to an unusual texture development where basal planes were almost perpendicular to the processed direction. The evolution of the texture after ECAP was similar in all the alloys.

  The ECAP produced a significant fragmentation of secondary phase particles in the WN43 and a homogeneous redistribution of these phases. Moreover, formation of new secondary phase particles was observed during the ECAP processing in the WN43 and N3 alloys.

- The evolution of the strength in compression was significantly affected by the grain refinement and an amount of alloying elements. The highest strength exhibits the WN43 under all investigated conditions which we attribute to the highest rate of grain refinement and to subsequent nucleation and redistribution of the fine secondary phase particles. Additionally, yttrium was considered as a great grain refiner.

  The microhardness evolution correlated with the compression deformation tests. We attribute the increase of hardness with the number of ECAP passes mainly to the grain boundary strengthening.

- The ECAP had almost no or slightly negative effect on the corrosion resistance of the N3 and WN43 alloys. However, in the case of the W3 significant increase of corrosion resistance with the increasing number of ECAP passes was measured. Presence of the intermetallic phases in magnesium matrix had accelerating effect during initial corrosion attack. Relatively

high amount of impurities (iron) in all three alloys probably influenced the corrosion resistance of solid solution samples.

It has been demonstrated that processing through ECAP can increase corrosion resistance in W3 alloy. Moreover, it can significantly increase mechanical strength of a material. Our results demand more research of W3 alloys as a promising material for medical application.

Bibliography

[1] LEHMHUS, D., BUSSE, M., HERRMANN, A., KAYVANTASH, K. (2013). *Structural Materials and Processes in Transportation,* John Wiley and Sons, Weinheim. ISBN 978-3-527-64986-0.

[2] SHEKHOVTSOV, G., SHCHEGOLEV, V., DEVYATKIN, V., TATAKIN A., ZABELIN, I. (2016). Magnesium Electrolytic Production Process. *LaTeX: Essential Readings in Magnesium Technology,* 97-100, ISBN 978-3-319-48588-1.

[3] WILLETT, E. (2007). *Magnesium - Understanding the elements of the periodic table,* The Rosen Publishing Group, New York. ISBN 978-1-4042-1007-3.

[4] DING, Y., WEN, C., HODGSON, P., LI, Y. (2014). Effects of alloying elements on the corrosion behavior and biocompatibility of biodegradable magnesium alloys: A review. *Journal of Materials Chemistry B,* **2**, 1912-1933.

[5] PEKGULERYUZ, M. O., KAINER, K., KAYA, A. A. (2013). *Fundamentals of Magnesium Alloy Metallurgy,* Woodhead Publishing Limited, Cambridge. ISBN 978-0-85709-729-3.

[6] MICHELS, W. (2000). *Magnesium alloys and their applications,* John Wiley and Sons, Weinheim. ISBN 978-3-527-30282-6.

[7] SONG, G. (2005). Recent Progress in Corrosion and Protection of Magnesium Alloys. *Advanced Engineering Materials,* **7**(7), 563-586.

[8] WITTE, F., HORT, N., VOGT, C., COHEN, S., KAINER, K. U., WILLUMEIT, R., FEYERABEND, F. (2008). Degradable biomaterials based on magnesium corrosion. *Current Opinion in Solid State and Materials Science,* **16**(6), 63-72.

[9] HIDALGO-MANRIQUE, P., ROBSON, J. D., PÉREZ-PRADO, M. T. (2017). Precipitation strengthening and reversed yield stress asymmetry in Mg alloys containing rare-earth elements: A quantitative study. *Acta Materialia,* **124**, 456-467.

[10] DA SILVA, E. P., BATISTA, L. F., CALLEGARI, B., BUZOLIN, R. H., WARCHOMICKA, F. G., REQUENA, G. C., ... PINTO, H. C. (2014). Solution and ageing heat treatments of ZK60 magnesium alloys with rare earth additions produced by semi-solid casting. *Materials research,* **17**(6), 1507-1512.

[11] ALANEME, K. K., OKOTETE, E. A. (2017). Enhancing plastic deformability of Mg and its alloys—A review of traditional and nascent developments. *Journal of Magnesium and Alloys,* **5**(4), 460-475.

[12] STANFORD, N., BARNETT, M. R., (2008). The origin of "rare earth" texture development in extruded Mg-based alloys and its effect on tensile ductility. *Materials Science and Engineering: A,* **496**(1), 399-408.

[13] QUACH, N.,UGGOWITZER, P. J., SCHMUTZ, P. (2008). Corrosion behaviour of an Mg–Y–RE alloy used in biomedical applications studied by electrochemical techniques. *Comptes Rendus Chimie,* **11**(9), 1043-1054.

[14] KUBÁSEK, J., VOJTĚCH, D. (2013). Structural and corrosion characterization of biodegradable Mg–RE (RE=Gd, Y, Nd) alloys. *Transactions of Nonferrous Metals Society of China,* **23**(5), 1215-1225.

[15] WINDHAGEN, H., RADTKE, K., WEIZBAUER, A., DIEKMANN, J., NOLL, Y., KREIMEYER, U., SCHAVAN, R., STUKENBORG-COLSMAN C. AND WAIZY H. (2013). Biodegradable magnesium-based screw clinically equivalent to titanium screw in hallux valgus surgery: short term results of the first prospective, randomized, controlled clinical pilot study. *BioMedical Engineering OnLine,* **12**(62). https://doi.org/10.1186/1475-925X-12-62.

[16] LIU, D., PAN, H., MENG, X. (2014). Mechanical properties of Mg–RE (RE = Sc, Y, Gd–Tm) solid solutions: first-principles determination. *Modelling and Simulation in Materials Science and Engineering,* **22**(5), 055017 (12pp).

[17] HÄNZI, A. C., GERBER, I., SCHINHAMMER, M., LÖFFLER, J. F., UGGOWITZER, P.J. (2010). On the in vitro and in vivo degradation performance and biological response of new biodegradable Mg–Y–Zn alloys. *Acta Biomaterialia,* **6**(5), 1824-1833.

[18] RIM, K. T., KOO, K. H., PARK, J. S. (2013). Toxicological Evaluations of Rare Earths and Their Health Impacts to Workers: A Literature Review. *Safety and Health at Work,* **4**(1), 12-26.

[19] ORLOV, D., JOSHI, V., SOLANKI, K. N., NEELAMEGGHAM,N. R. (2018). *LaTeX: Magnesium Technology 2018,* Springer. ISBN 978-3-319-72332-7.

[20] LING, W. (2006). Effect of Neodymium on Microstructure and Mechanical Properties of Mg-Sb Alloy. *Journal of Rare Earths,* **24**(1), 376-378.

[21] MORGAN, J. E., MORDIKE, B. L. (1981). An investigation into creep-resistant, as-cast magnesium alloys containing yttrium, zinc, neodymium and zirconium. *Metallurgical Transactions A,* **12**(9), 1581-1585.

[22] LIU, N., WANG, J., WANG,L., WU, Y., WANG, L. (2009). Electrochemical corrosion behavior of Mg–5Al–0.4Mn–xNd in NaCl solution. *Corrosion Science,* **51**(6), 1328-1333.

[23] TEKUMALLA, S., SEETHARAMAN, S., ALMAJID, A. AND GUPTA, M. (2015). Mechanical Properties of Magnesium-Rare Earth Alloy Systems: A Review. *Metals,* **5**, 1-39.

[24] ZHANG, Y., ZENG, X., LIU, L., LU, C., ZHOU, H.,LI, Q.,ZHU, Y. (2004). Effects of yttrium on microstructure and mechanical properties of hot-extruded Mg–Zn–Y–Zr alloys. *Materials Science and Engineering A,* **373**(1), 320-327.

[25] CHEN, T. J., ZHANG, D. H., WANG, W., MA, Y. AND HAO, Y. (2016). Effects of Nd or Zr Addition on Microstructure and Mechanical Properties of As-Cast Mg-Zn-Y Alloy. *Materials Transactions,* **57**(8), 1287-1295 .

[26] NIE, J. F. (1998). Precipitation and Hardening in Magnesium Alloys.*Metallurgical and Materials Transactions A,* **5**, 1589-1599.

[27] NIE, J. F. AND MUDDLE, B.C. (2000). Characterization of strengthening precipitate phases in a Mg-Y-Nd alloys. *Acta Materialia,* **48**, 1691-1703.

[28] ANTION, C., DONNADIEU, P., PERRARD, F., DESCHAMPS, A., TASSIN, C., PISCH, A. (2003). Hardening precipitation in a Mg-4Y-3RE alloy. *LaTeX: Acta Materialia,* **51**, 5335-5348.

[29] DROZDENKO, D., BOHLEN, J., CHMELÍK, F., LUKÁČ, P., DOBROŇ,P. (2016). Acoustic emission study on the activity of slip and twin mechanisms during compression testing of magnesium single crystals. *Materials Science and Engineering A,* **650**, 20-27.

[30] LANGDON, T. G. (2013). Twenty-five years of ultrafine-grained materials: Achieving exceptional properties through grain refinement. *Acta Materialia,* **61**(19), 7035-7059.

[31] VALIEV, R. Z., LANGDON, T.G. (2006). Principles of equal-channel angular pressing as a processing tool for grain refinement. *Progress in Materials Science,* **51**, 881-981.

[32] QARNI, M. J., ROSOCHOWSKI, A. AND BOCZKAL, S. (2017). Influence of incremental ECAP on the microstructure and tensile behaviour of commercial purity titanium. *Procedia Engineering,* **207**, 1481-1486.

[33] NAKASHIMA, K., HORITA, Z., NEMOTO, M., LANGDON, T.G. (1998). Influence of channel angle on the development of ultrafine grains in equal-channel angular pressing. *Acta Materialia,* **46**(5), 1589-1599.

[34] MINÁRIK, P., LANDA, M., LESNÁ, I.K., ZEMKOVÁ, M., JABLONSKÁ, E., HADZIMA, B., JANECEKA, M., KRÁL, R. (2015). Interrelation of Microstructure and Corrosion Resistance in Biodegradable Magnesium Alloys with Aluminum, Lithium and Rare Earth Additions. *Acta Physica Polonica A,* **128**(4), 491-495.

[35] AVEDESIAN, M. M., BAKER, H. (1999). *ASM Specialty Handbook: Magnesium and Magnesium Alloys,* ASM International, Materials Park. ISBN: 978-0-87170-657-7.

[36] XIN, R., LI, B., LI,L., LIU, Q. (2011). Influence of texture on corrosion rate of AZ31 Mg alloy in 3.5 wt.% NaCl. *Materials & Design,* **32**(8), 4548-4552.

[37] ZHENG, Y. (2016). *Magnesium alloys as degradable biomaterials,* Taylor and Francis Group, Boca Raton. ISBN 978-1-4665-9806-5.

[38] WAIZY, H., DIEKMANN, J., WEIZBAUER, A., REIFENRATH, J., BARTSCH, I., NEUBERT, V., SCHAVAN, R., WINDHAGEN, H. (2014). In vivo study of a biodegradable orthopedic screw (MgYREZr-alloy) in a rabbit model for up to 12 months. *Journal of Biomaterials Applications,* **24**(5), 667-675.

[39] *LaTeX: Manual OIM data collection, http://www.material.ntnu.no/ebsd/EBSD/OIM%20Analysis%205_3%20%20Manual.pdf.*

[40] ILLKOVÁ, K. (2013). *LaTeX: Doctoral Thesis: Influence of Solid Solution Elements and Precipitate Formation on the Mechanical Behaviour of Magnesium Alloys.*

[41] *Metrohm-AUTOLAB Application Notes, https://www.metrohm.com/en/applications/AN-COR-003.*

[42] HOU, X. L., ZHAI, Y. X., ZHANG, P., GUO, S., YUAN, Z. Z., GUAN, Q. F. (2016). Rare earth texture analysis of rectangular extruded Mg alloys and a comparison of different alloying adding ways. *Rare Metals,* **35**(11), 850-857.

[43] HIDALGO-MANRIQUE, P., YI, S. B., BOHLEN, J., LETZIG, D., PÉREZ-PRADO, M. T. (2013). Effect of Nd Additions on Extrusion Texture Development and on Slip Activity in a Mg-Mn Alloy. *Metallurgical and Materials Transactions A,* **44**(10), 4819-4829.

[44] ZEMKOVÁ, M., DROZDENKO, D., BOHLEN, J., MINÁRIK, P. (2018). CHARACTERIZATION OF MICROSTRUCTURE AND MECHANICAL PROPERTIES OF MAGNESIUM ALLOYS WITH NEODYMIUM AND YTTRIUM PROCESSED BY EXTRUSION. *METAL 2017 Conference Proceedings* Brno, 2017, 1531-1536. Ostrava: TANGER Ltd.

[45] ZEMKOVÁ, M., KRÁL, R., BOHLEN, J., ČAPEK, J., HADZIMA, B., MINÁRIK, P. Investigation of mechanical properties and microstructure of non-commercial magnesium alloy prepared by extrusion and ECAP. Submitted to International Journal Acta Physica Polonica A.

[46] MINÁRIK, P., VESELÝ, J., KRÁL, R., BOHLEN, J., KUBÁSEK, J., JANEČEK, M. (2017). Exceptional mechanical properties of ultra-fine grain Mg-4Y-3RE alloy processed by ECAP. *Materials Science and Engineering: A,* **708**, 193-198.

[47] ZHOU, L., LIU, Y., ZHANG J., KANG, Z. (2016). Microstructure and mechanical properties of equalchannel angular pressed Mg–Y–RE–Zr alloy. *Materials Science and Technology,* **32**(10), 969-975.

[48] MINÁRIK, P., KRÁL, R., ČÍŽEK, J., CHMELÍK, F. (2016). Effect of different c/a ratio on the microstructure and mechanical properties in magnesium alloys processed by ECAP. *Acta Materialia,* **107**, 83-95.

[49] CHANG, H.-W., QIU, D., TAYLOR, J. A., EASTON, M. A., ZHANG, M.-X. (2013). The role of Al2Y in grain refinement in Mg–Al–Y alloy system. *Journal of Magnesium and Alloys,* **1**(2), 115-121.

[50] JANEČEK, M., YI ,S.,KRÁL R., VRÁTNÁ, J., KAINER, K.U. (2010). Texture and microstructure evolution in ultrafine-grained AZ31 processed by EX-ECAP. *Journal of Materials Science,* **45**, 4665-4671.

[51] ANDO, S., KODERA, A., FUKUSHIMA, K., TSUSHIDA, M., KITAHARA, H. (2014). Tensile deformation of magnesium and magnesium alloy single crystals. *Materials Science Forum,* **783-786**, 341-345.

[52] GRIFFITHS, D. (2015). Explaining texture weakening and improved formability in magnesium rare earth alloys. *Materials Science and Technology,* **31**(1), 10-24.

[53] GAO, L., CHEN, R.S., HAN, E.H. (2009). Solid solution strengthening behaviors in binary Mg–Y single phase alloys. *Journal of Alloys and Compounds,* **472**, 234-240.

[54] HIDALGO-MANRIQUE, P., YI, S. B., BOHLEN, J., LETZIG, D., PÉREZ-PRADO, M. T. (2013). Effect of Nd Additions on Extrusion Texture Development and on Slip Activity in a Mg-Mn Alloy. *Metallurgical and Materials Transactions A,* **44**(10), 4819-4829.

[55] KIM, H.K., KIM, W.J. (2004). Microstructural instability and strength of an AZ31 Mg alloy after severe plastic deformation. *Materials Science and Engineering: A,* **385**(1–2), 300-308.

[56] ZHANG, X., ZHANG, K., LI, X., DENG, X., LI, Y., MA, M., SHI, Y. (2012). Effect of solid-solution treatment on corrosion and electrochemical behaviors of Mg-15Y alloy in 3.5 wt.% NaCl solution. *Journal of rare earth,* **30**(11), 1158-1167.

[57] OP'T HOOG, C., BIRBILIS, N. AND ESTRIN, Y. (2008). Corrosion of Pure Mg as a Function of Grain Size and Processing Route. *Advanced enginnering materials,* **10**(6), 579-583.

[58] IZUMI, S., YAMASAKI, M., KAWAMURA, Y. (2009). Relation between corrosion behavior and microstructure of Mg–Zn–Y alloys prepared by rapid solidification at various cooling rates. *Corrosion Science Volume,* **51**(2), 395-402.

[59] MINÁRIK, P., KRÁL, R., JANEČEK, M. (2013). Effect of ECAP processing on corrosion resistance of AE21 and AE42 magnesium alloys. *Applied Surface Science,* **281**, 44-48.

[60] HANG, L. -N., HOU, Z. -T., YE, X., XU, Z. -B., BAI, X. -L. AND SHANG, P. (2013). The effect of selected alloying element additions on properties of Mg-based alloy as bioimplants: A literature review. *Frontiers of Material Science,* **7**(3), 227-236.

[61] CHINO, Y., HOSHIKA, T. AND MABUCHI, M. (2006). Mechanical and Corrosion Properties of AZ31 Magnesium Alloy Repeatedly Recycled by Hot Extrusion. *Materials Transactions,* **47**(4), 1040-1046.

[62] SONG, G. AND ATRENS, A. (2003). Understanding Magnesium Corrosion A Framework for Improved Alloy Performance. *Advanced enginnering materials,* 5(12), 837-858.

List of Figures

List of Tables